Eddy–Mean Flow Interaction in the Gulf Stream at 68°W. Part I: Eddy Energetics*

MEGHAN CRONIN AND D. RANDOLPH WATTS

Graduate School of Oceanography, University of Rhode Island, Kingston, Rhode Island

(Manuscript received 23 March 1994, in final form 22 February 1995)

ABSTRACT

From June 1988 to August 1990 twelve tall, high-performance, current meter moorings measured the Gulf Stream's velocity and temperature fields at nominal depths of 400 m, 700 m, 1000 m, and 3500 m along three lines centered at 68°W. The overall eddy variability during the 26-month experiment was dominated by six large amplitude trough formation events, with each event lasting approximately one month. To determine the source(s) of energy for this eddy variability, the eddy energy budget is evaluated. Traditionally, the baroclinic conversion of mean potential energy to eddy potential energy is defined as a downgradient heat flux. However, because a nondivergent heat flux can be downgradient even under conditions in which there is no baroclinic conversion occurring, a better, more dynamically correct definition of a baroclinic conversion rate is a downgradient horizontally divergent heat flux. The horizontally divergent heat flux component is estimated to be approximately half the full horizontal heat flux vector. Nevertheless, the resulting "dynamical" baroclinic conversion rate is found to be positive and nearly an order of magnitude larger than the weakly positive barotropic conversion rate. Because the large troughs at 68°W are formed through a baroclinic conversion process, the Gulf Stream jet is judged to be baroclinically unstable at 68°W.

1. Introduction

As the Gulf Stream flows offshore from the continental margin near Cape Hatteras, the meanders in the path grow in amplitude from rms values of 10 km at 74°W to 40 km at 69°W. At 70°–69°W, there is a local minimum in the meander envelope, called a "meander node" (Cornillon 1986; Kontoyiannis and Watts 1994), while east of 69°W the meanders can become large amplitude and convoluted, sometimes pinching off to form cyclonic cold core and anticyclonic warm core rings (Watts 1983). In an effort to understand the physics of this variability, an intensive Gulf Stream modeling and observational field program, the Synoptic Ocean Prediction (SYNOP) program was initiated (Watts 1985). As a part of the SYNOP field program, two current meter arrays measured and mapped the flow and mass fields at 68°W (Watts et al. 1995) and 55°W (Hogg 1992) with sufficient duration and resolution to analyze the Gulf Stream eddy–mean flow interaction. In this paper, the eddy energy budget is evaluated using data from the 68°W array. In the companion paper (Cronin 1996) (hereinafter called Part II), the effects of these eddies on the mean flow are evaluated.

The purpose in evaluating the eddy energy budget is twofold. Because the energy budget involves the gradients in the mean fields, and variances and covariances of the temperature and velocity fields, an energetics analysis provides a benchmark for models trying to reproduce the observed variability. The error estimates in this analysis are measurement errors rather than statistical errors and reflect the array's ability to interpolate and extrapolate the measurements horizontally, and thus create a field which can be mapped. Nevertheless, we believe that the statistical fields might represent the long-term fields. The study region is characterized by large amplitude trough events. During the 26-month record, six large amplitude trough events formed locally and a trough feature is evident in the upper level 26-month averaged fields. A similar trough feature is also evident in the 93-month average satellite IR SST field (Lee 1994). Work is currently underway to investigate the life cycle of these large amplitude trough formation events.

Besides being useful as a benchmark, the energetics analysis can be used as a diagnostic analysis to identify dynamical processes responsible for the observed variability, such as for the large amplitude troughs which formed in the 68°W study region. Commonly, if the dynamical process is suspected to be a hydrodynamic instability, the barotropic and baroclinic conversion rates are compared to determine the dominance of baroclinic and/or barotropic instabilities. However, as dis-

* NOAA Pacific Marine Environmental Laboratory Contribution Number 1684.

Corresponding author address: Dr. Meghan Cronin, NOAA/PMEL, 7600 Sand Point Way, NE, Bin C15700, Seattle, WA 98115-0070.

cussed by Pedlosky (1987), a problem with the eddy–mean flow instability analysis is that the mean field tends to be more stable than the initial unperturbed field since the mean field is broadened by the eddies and has weaker gradients.

A more subtle and potentially more problematic aspect of the temporal-mean eddy–flow interaction analysis is that only the horizontally divergent eddy heat fluxes should be directly related to heat advection events such as baroclinic instability events. However, traditionally the rate of mean to eddy potential energy conversion is estimated by the downgradient heat flux, with no distinction as to whether the fluxes are horizontally divergent or nondivergent. As discussed by Marshall and Shutts (1981), inclusion of the nondivergent component of the heat flux in the baroclinic conversion rate can lead to a nonzero rate even under conditions in which no baroclinic conversion has occurred.

To take greater advantage of the dynamical information in the eddy energy budget, the derivation and interpretation of an energetics analysis will be reviewed in section 2. In section 3, the experiment and the method used for obtaining high quality maps of the temperature field and maps of the velocity and associated streamlines of flow are described. In section 4, the mean and eddy fields are presented and the divergent heat fluxes are evaluated using a method developed by Marshall and Shutts (1981). This method, which is based on approximating temperature contours as geostrophic streamlines, requires maps of the temperature and flow field and maps of the mean field streamlines. Use of this method has been limited thus far to atmospheric analyses (Illari and Marshall 1983). In section 5, the eddy energy budgets are evaluated, and the results are summarized in section 6 and discussed in section 7.

2. Dynamics governing variability

Upstream of the SYNOP study region, at 73°W, Johns et al. (1989) demonstrated that the quasigeostrophic (QG) assumption was valid below about 200 m. At the SYNOP 68°W study region, the Rossby number $\mathrm{Ro} = U/f_0L$ at 400 m is typically 0.05–0.15 ($U \sim 1$–$1.5\ \mathrm{m\ s^{-1}}$, $f \sim 10^{-4}\ \mathrm{s^{-1}}$, $L \sim 100$–200 km), with peak values of up to 0.35 ($U \sim 1.75\ \mathrm{m\ s^{-1}}$, $L \sim 50$ km), while at 700 m and deeper, where the flow is weaker, the typical and peak values of Ro are much less than 0.1 and 0.35. While a QG predictive model might be marginal at 400 m, for diagnostic purposes the QG dynamics still ellucidate the main balances. Thus, this analysis of the eddy dynamics and eddy energetics will be entirely within the QG framework.

By the QG assumption, the total three-dimensional flow $\mathbf{U} = (U, V, w)$ can be decomposed into an $O(1)$ geostrophic component $\mathbf{u} = (u, v, 0)$ and a small $O(\mathrm{Ro})$ ($\mathrm{Ro} \ll 1$) ageostrophic component $\mathbf{U}_a = (u_a, v_a, w)$:

$$\mathbf{U} = \mathbf{u} + \mathbf{U}_a \approx \mathbf{u}$$

$$\mathbf{u} = \hat{\mathbf{z}} \times \nabla \frac{1}{f_0\rho_0} P,$$

where all quantities are in dimensional units, $(\hat{\mathbf{x}}, \hat{\mathbf{y}}, \hat{\mathbf{z}})$ are the unit vectors directed eastward, northward, and upward, ∇ is the horizontal gradient operator,

$$\nabla = \left(\hat{\mathbf{x}} \frac{\partial}{\partial x}, \hat{\mathbf{y}} \frac{\partial}{\partial y}\right),$$

ρ_0 is the volume-averaged density, P is pressure, and f_0 is the Coriolis parameter evaluated at a central latitude. Hereinafter, temperature will be used as a proxy for density $\rho = \rho_0(1 - \alpha T)$. In order that the quasi-horizontal flow conserve heat, by the QG assumption, the temperature surfaces cannot be too sharply tilted. The temperature field can therefore be decomposed into a depth-dependent background field $\theta(z)$ and a dynamically important, weakly varying field $\delta T(x, y, z, t)$:

$$T(x, y, z, t) = \theta(z) + \delta T(x, y, z, t).$$

By the QG assumption, the stability of the fluid is approximated by the background stratification: $|\theta_z| \gg |(\delta T)_z|$. Additionally, by the beta-plane approximation, the Coriolis parameter is approximated as $f = f_0 + \beta y$, where $|f_0| \gg |\beta y|$.

Thus, the $O(1)$ QG momentum equations, the geostrophic and hydrostatic equations, in dimensional units are

$$f_0\hat{\mathbf{z}} \times \mathbf{u} = -\frac{1}{\rho_0} \nabla P \tag{1}$$

$$0 = -\frac{1}{\rho_0} \frac{\partial P}{\partial z} + g\alpha\delta T. \tag{2}$$

The variability in this $O(1)$ geostrophic flow $\mathbf{u}$ is controlled by the $O(\mathrm{Ro})$ momentum, heat, and continuity equations:

$$\frac{\partial \mathbf{u}}{\partial t} + \mathbf{u}\cdot\nabla\mathbf{u} + \beta y\hat{\mathbf{z}} \times \mathbf{u} + f_0\hat{\mathbf{z}} \times \mathbf{u}_a = 0 \tag{3}$$

$$\frac{\partial \delta T}{\partial t} + \mathbf{u}\cdot\nabla\delta T + w\theta_z = 0 \tag{4}$$

$$\nabla\cdot\mathbf{u}_a = -\frac{\partial w}{\partial z}, \tag{5}$$

where $O(\mathrm{Ro}^2)$ terms have been neglected. These equations (1)–(5) comprise the QG governing equations of motion (Gill 1982).

Defining the eddy field to be the deviation from the time-mean field, the geostrophic flow $\mathbf{u}$ and ageostrophic flow $\mathbf{U}_a$ can each be decomposed into time mean and eddy components:

$$\mathbf{u} = \bar{\mathbf{u}} + \mathbf{u}'$$

$$\mathbf{U}_a = \bar{\mathbf{U}}_a + \mathbf{U}_a',$$

where the overline designates the time-averaging operator. Note that although both components of the ageostrophic flow field are small to $O(\mathrm{Ro})$, the geostrophic perturbation flow $\mathbf{u}'$ is not necessarily smaller than the mean flow $\bar{\mathbf{u}}$. The time-mean eddy decomposition can also be applied to the dynamical portion of the mass field δT:

$$\delta T = \Delta T(x, y, z) + T'(x, y, z, t),$$

where $\bar{T} = \theta(z) + \Delta T(x, y, z)$, and by QG scaling,

$$\left| \frac{\partial}{\partial z} \Delta T \right| \ll |\theta_z|,$$

and

$$\left| \frac{\partial}{\partial z} T' \right| \ll |\theta_z|.$$

The QG equations governing variability in $\mathbf{u}'$ can be derived by subtracting the time average of (1)–(5) from the full equations (1)–(5). Because this is an intermediary step for deriving the eddy energetics, these perturbation equations will not be presented. Nevertheless, for interpreting the statistical budgets, it is important to note that because $\mathbf{u}$, $\bar{\mathbf{u}}$, and $\mathbf{u}'$ are each horizontally nondivergent, the heat advection by the geostrophic eddy field is associated with horizontally divergent heat fluxes:

$$-\mathbf{u}' \cdot \nabla T' = -\nabla \cdot \mathbf{u}' T'.$$

In other words, *horizontally nondivergent heat fluxes* are not related to *heat advection* (e.g., *baroclinic conversion*) events. This qualification remains true even when the fluxes are time averaged:

$$-\overline{\mathbf{u}' \cdot \nabla T'} = -\nabla \cdot \overline{\mathbf{u}' T'}^{\mathrm{div}}.$$

Thus, care must be taken when interpreting dynamics in terms of statistics: Only the divergent component of the heat flux should be interpreted in terms of heat advection events such as baroclinic instability events.

a. Derivation of the EPE budget

The mean budget for the eddy potential energy

$$\mathrm{EPE} = \frac{g\alpha}{2\theta_z} \overline{T'^2}$$

can be derived by time averaging the heat equation (4) multiplied by the factor $g\alpha T'/\theta_z$. Assuming that to $O(\mathrm{Ro})$, α is only a function of depth [recall $\theta = \theta(z)$], then the EPE budget can be written as

$$0 = \underbrace{-\bar{\mathbf{u}} \cdot \nabla \mathrm{EPE}}_{\mathrm{MAP}} \underbrace{- \nabla \cdot \overline{\mathbf{u}' \mathrm{EPE}'}}_{\mathrm{EAP}} \underbrace{- \frac{g\alpha}{\theta_z} \overline{\mathbf{u}' T'} \cdot \nabla \bar{T}}_{\mathrm{BC}} \underbrace{- g\alpha \overline{T' w'}}_{-\mathrm{PKC}}, \quad (6)$$

where

$$\mathrm{EPE}' = \frac{g\alpha}{2\theta_z} T'^2$$

is not yet time averaged. Because this is a steady-state balance, at each location there is a balance between the mean advection of EPE (MAP), the eddy advection of EPE (EAP), and the horizontal (BC) and vertical (−PKC) downgradient heat fluxes. Although this form of the EPE budget is useful as a benchmark for model integrity, it makes no distinction between divergent and nondivergent heat fluxes and therefore is difficult to interpret in terms of dynamical processes.

A baroclinic conversion process is essentially a heat advection process that lowers the center of mass of the fluid. Because only the horizontally divergent heat fluxes can be associated with heat advection events, following Illari and Marshall (1983), a dynamical baroclinic conversion rate can be defined as a downgradient horizontally divergent heat flux:

$$\text{dynamical BC conversion rate} = -\frac{g\alpha}{\theta_z} \overline{\mathbf{u}' T'}^{\mathrm{div}} \cdot \nabla \bar{T}. \quad (7)$$

Marshall and Shutts (1981) provide a method (hereinafter called the MS method) for decomposing the time-averaged heat flux field into a purely horizontally nondivergent component and a residual "divergent" component. Briefly, since the geostrophic velocity can be related to a streamfunction: $\mathbf{u} = \hat{\mathbf{z}} \times \nabla\psi$, if the mean streamlines are nearly parallel to the mean temperature contours such that $\bar{\psi} \approx \bar{\psi}(\bar{T})$, then the factor $d\bar{\psi}/d\bar{T}$ can be used to define a velocity $\bar{\mathbf{u}}_{\|}$, which flows along mean temperature contours and does not advect mean temperature:

$$\bar{\mathbf{u}}_{\|} = \hat{z} \times \nabla \frac{d\bar{\psi}}{d\bar{T}} \bar{T}.$$

The component of the mean flow that is responsible for the mean heat advection is in the residual mean flow $\bar{\mathbf{u}}_{\perp} \approx \bar{\mathbf{u}} - \bar{\mathbf{u}}_{\|}$. Assuming the empirical factor $d\bar{\psi}/d\bar{T}$ can be applied to the instantaneous field, a perturbation velocity $\mathbf{u}'_{\|}$ that is parallel to T' contours can similarly be defined:

$$\mathbf{u}'_{\|} = \hat{\mathbf{z}} \times \nabla \frac{d\bar{\psi}}{d\bar{T}} T'.$$

The eddy heat flux by $\mathbf{u}'_{\|}$ is purely horizontally nondivergent:

$$\overline{\mathbf{u}'_{\|} T'} = \hat{\mathbf{z}} \times \overline{T' \nabla \frac{d\bar{\psi}}{d\bar{T}} T'} = \hat{\mathbf{z}} \times \nabla \frac{1}{2} \frac{d\bar{\psi}}{d\bar{T}} \overline{T'^2} = \overline{\mathbf{u}' T'}^{\mathrm{nondiv}} \quad (8)$$

and by definition is not related to temperature advection events. The divergent component of the heat flux field, which is related to heat advection events, is contained in the residual eddy heat flux

$$\overline{\mathbf{u}'T'}^{\text{div}} \approx \overline{\mathbf{u}'T'} - \overline{\mathbf{u}'T'}^{\text{nondiv}}. \tag{9}$$

Caution is warranted in using (9) to estimate the divergent flux field since if (8) does not capture the full horizontally nondivergent field, then the residual flux will not be purely divergent. Thus, with closed boundary conditions, it might be preferable to determine the purely horizontally divergent and nondivergent flux fields by solving the Poisson equation, as was done by Lau and Wallace (1979).

Returning to the EPE budget, MS show that there is internal canceling between the downgradient heat flux and the mean advection of EPE: Noting that

$$\bar{\mathbf{u}}_{\|} = \frac{d\bar{\psi}}{d\bar{T}}\hat{\mathbf{z}} \times \nabla\bar{T},$$

and multiplying the vector identity

$$(\hat{\mathbf{z}} \times \nabla\bar{T})\cdot\nabla\overline{T'^2} = -(\hat{\mathbf{z}} \times \nabla\overline{T'^2})\cdot\nabla\bar{T}$$

by the factor

$$\frac{g\alpha}{2\theta_z}\frac{d\bar{\psi}}{d\bar{T}},$$

MS and Illari and Marshall (1983) show that the mean advection of EPE by $\bar{\mathbf{u}}_{\|}$ balances the downgradient nondivergent heat flux:

$$\bar{\mathbf{u}}_{\|}\cdot\nabla\text{EPE} = -\frac{g\alpha}{\theta_z}\overline{\mathbf{u}'_{\|}T'}\cdot\nabla\bar{T}$$

$$= -\frac{g\alpha}{\theta_z}\overline{\mathbf{u}'T'}^{\text{nondiv}}\cdot\nabla\bar{T}. \tag{10}$$

Thus, assuming that the MS method (8)–(9) accurately decomposed the heat flux field into purely horizontally divergent and nondivergent components, then by explicitly canceling the internal balance (10) in the EPE budget (6),

$$0 = \overbrace{-\bar{\mathbf{u}}_{\perp}\cdot\nabla\text{EPE}}^{\text{dynMAP}} - \overbrace{\frac{g\alpha}{\theta_z}\overline{\mathbf{u}'T'}^{\text{div}}\cdot\nabla\bar{T}}^{\text{dynBC}}$$

$$\overbrace{-\nabla\cdot\overline{\mathbf{u}'\text{EPE}'}}^{\text{EAP}} \overbrace{-g\alpha\overline{T'w'}}^{-\text{PKC}}, \tag{11}$$

each term can be directly related to temperature advection events and true baroclinic conversion processes.

b. Derivation of the EKE budget

The EKE budget is obtained by time averaging the scalar product of the eddy velocity vector and the eddy momentum equations, $\overline{\mathbf{u}'\cdot(\text{eqn3})} + \overline{w'(\text{eqn2})}$:

$$0 = \overbrace{-\bar{\mathbf{u}}\cdot\nabla\text{EKE}}^{\text{MAK}} \overbrace{-\nabla\cdot\overline{\mathbf{u}'\text{EKE}'}}^{\text{EAK}}$$

$$\overbrace{-\left(\overline{u'u'}\frac{\partial\bar{u}}{\partial x} + \overline{u'v'}\left(\frac{\partial\bar{u}}{\partial y} + \frac{\partial\bar{v}}{\partial x}\right) + \overline{v'v'}\frac{\partial\bar{v}}{\partial y}\right)}^{\text{BT}}$$

$$\underbrace{-\overline{\frac{\mathbf{u}'_a}{\rho_0}\cdot\nabla P'}}_{\text{horPW}} \underbrace{-\overline{\frac{w'}{\rho_0}\frac{\partial P'}{\partial z}}}_{\text{vertPW}} + \underbrace{g\alpha\overline{w'T'}}_{\text{PKC}}, \tag{12}$$

where $\text{EKE}' = (u'u' + v'v')/2$ is not yet time averaged and the geostrophic relation has been substituted for $\mathbf{u}'$:

$$f_0\overline{\mathbf{u}'\cdot\hat{\mathbf{z}}\times\mathbf{u}'_a} = \overline{\mathbf{u}'_a\cdot\nabla\frac{P'}{\rho_0}}.$$

Thus, the steady-state EKE budget comprises a balance between the mean advection of EKE (MAK), the eddy advection of EKE (EAK), horizontal momentum fluxes that are oriented down the mean momentum gradient (BT), horizontal and vertical eddy pressure work by the ageostrophic flow (horPW and vertPW), and vertical heat fluxes (PKC). Although by the hydrostatic relation, the vertical heat flux (i.e., the EPE to EKE conversion rate) identically balances the vertical eddy pressure work term (vertPW + PKC = 0), these terms are important in the EKE budget since they couple the mass field and the flow field: The redistribution of the mass field, which results in a vertical heat flux, changes the local hydrostatic pressure, and therefore the horizontal pressure gradient, and results in pressure work being done on the eddy flow.

Traditionally the downgradient momentum flux BT is interpreted as the rate of barotropic conversion from MKE to EKE. Although Plumb (1983) shows that alternate expressions can be defined to represent energy exchange rates between the MKE and EKE equations, the traditional definition appears to be dynamically well grounded. There is no analog for the MS decomposition since the momentum fluxes form a tensor rather than a vector. Furthermore, the traditional barotropic conversion rate is consistent with the theory of eddy forcing of the time-mean flow, which is developed in Part II. Therefore, the traditional definition of the barotropic conversion rate will be used.

3. The data

As part of the SYNOP program, for two years from June 1988 to August 1990, 12 moorings arranged along three lines centered at 68°W measured temperature and velocity at the nominal depths of 400 m, 700 m, 1000

m, and 3500 m (Shay et al. 1992). Three of the central moorings were also mounted with an upward looking ADCP (Johns and Zantopp 1991) that provided data redundancy at the 400-m level. As shown in Fig. 1, the mooring array was imbedded within a larger array of inverted echo sounders (IESs) and IESs at the base of the moorings were equipped with pressure sensors (Tracey and Watts 1991). IESs are bottom-moored acoustic instruments from which the depth of the main thermocline (i.e., the depth of the 12°C isotherm) can be determined (Watts and Rossby 1977). As discussed in appendix A, we were able to use the IESs to also determine the temperature at 400, 700, and 1000 m. The current meter and IES array design, measurements, data return, and processing are summarized in Shay et al. (1995) and Watts et al. (1995). To remove inertial and tidal fluctuations, all measurements were 40-hour low-pass filtered. Because the mooring and IES spacing (56 km in cross stream and 65 km in downstream) is less than the path correlation length scale, the IES/current meter array resolves the mesoscale and larger-scale eddy structure.

As a first step toward creating regularly gridded data, the upper-level mooring measurements were interpolated (and extrapolated) to fixed depths of 400, 700, and 1000 m using a mooring motion correction scheme adapted from Hogg (1991). Details of the mooring motion correction scheme can be found in appendix A and in Cronin et al. (1992). The constant horizon (400, 700, 1000, and 3500 m) temperature and velocity measurements were mapped onto a 260 km north–south by 200 km east–west grid with 10 km spacing using optimal interpolation (OI) (Bretherton et al. 1976; Freeland and Gould 1976).

In mapping the velocities, it was assumed that the velocity components at all levels were horizontally nondivergent: $\mathbf{u} = \hat{\mathbf{z}} \times \nabla\psi$, where ψ is the streamfunction of flow. At 3500 m, pressure measurements were available and it was also assumed that the flow was geostrophic: $\mathbf{u} = \hat{\mathbf{z}} \times \nabla P/(\rho_0 f_0)$. Thus, for each level, an autocorrelation function of the streamfunction could be used together with the measured u, v, and P (where available) to create a gridded field of nondivergent velocities and streamfunctions of flow. Since Kim and Watts (1994) have shown that IES 12°C isotherm (Z_{12}) contours can act as baroclinic streamlines of flow, in the upper layer the streamline correlation function was based on the IES Z_{12} correlation function (Tracey and Watts 1991). In the deep layer, a pressure correlation function was estimated from the data (Qian and Watts 1992). At all levels in this study, the mapped nondivergent velocities are treated as geostrophic estimates.

The OI also estimates and maps the fractional error based on the relative size of the combined measurement and ageostrophic noise, the correlation length scale and instrument spacing, and the types of input data (e.g., velocity or velocity and pressure). As discussed in appendix B, these (u, v, T) error variance maps can be

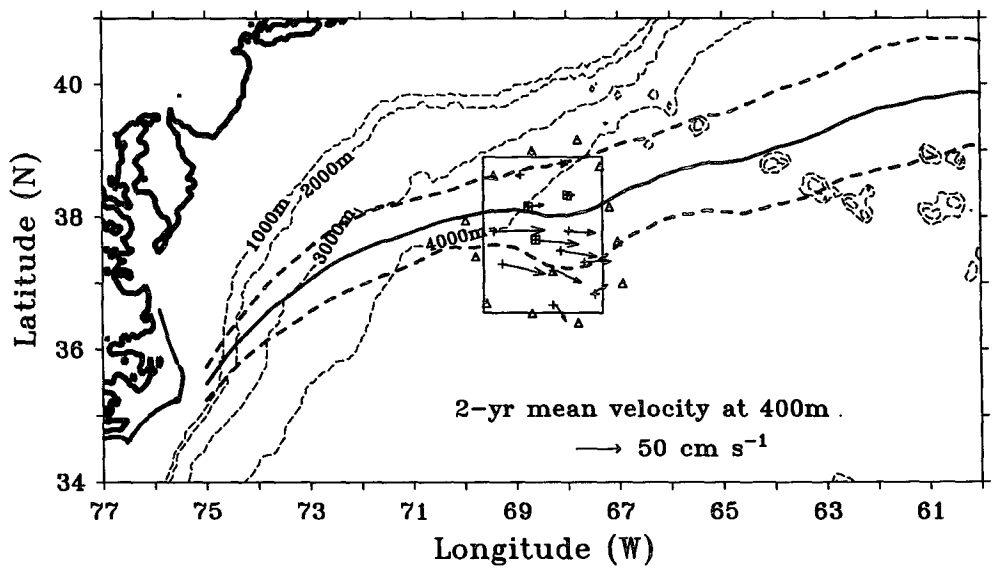

FIG. 1. The boxed study region shows the area in which the measured fields are mapped. Plus marks indicate mooring sites. Triangles indicate inverted echo sounder sites used to estimate temperature at 400, 700, and 1000 m. Squares indicate moorings with an additional upward looking ADCPs. The mean Gulf Stream path (thick solid line) and the ±1 standard deviation envelope (thick dashed lines) are computed from 93 months of satellite IR images (Lee 1994). Twelve moorings were in place during the first deployment year. During the second deployment year a 13th mooring between the second and third lines was set in place; however two critical instruments on the second most southern mooring along the second line failed during the second year. Thus, although 13 moorings are shown in Fig. 1, only 12 obtained useful data for each of the two years.

used to create error maps for the computed energy transfer rates. Further details of the OI scheme used to map the upper level u, v, T, ψ fields can be found in Cronin (1993); Qian and Watts (1992) document the OI scheme used to map the 3500-m level u, v, T, p fields.

4. The Gulf Stream's mean and eddy fields at 68°W

During the 26-month experiment, the Gulf Stream at 68°W experienced approximately 28 propagating meanders, 2–4 warm core ring–stream interactions, 2 cold core ring–stream interactions, and 6 steep troughs (one of which pinched off to form a cold core ring). Of these events, the six steep trough events are the most energetic, each lasting approximately a month. An example of one of these troughs is shown in Fig. 2. This steep trough has a wavelength of approximately 240 km and an amplitude of 80 km. Almost all moorings show a consistent pattern of temperature advection, with cold advection west of the flow field trough axis and warm advection east of the flow field trough. This pattern of heat advection is consistent with the temperature wave lagging the streamline wave and is indicative of a classic baroclinic instability disturbance (e.g., Charney 1947; Eady 1949).

The mean and eddy fields and energy transfer rates are inherently related to the six large amplitude troughs that formed in the study region. As can be seen in Fig. 3a, the mean temperature and flow fields show a trough pattern that is evident in the 700-m and 1000-m levels. Curiously, the mean deep velocities show a deep cyclone beneath the upper level trough axis. The mechanism by which the eddies (i.e., the troughs) sustain this time-mean deep cyclonic circulation is the focus of Part II. As can also be seen in Fig. 3b, the temperature variance fields at all levels have a local maximum centered along the trough axis near the eastern edge of the array at 67.5°W.

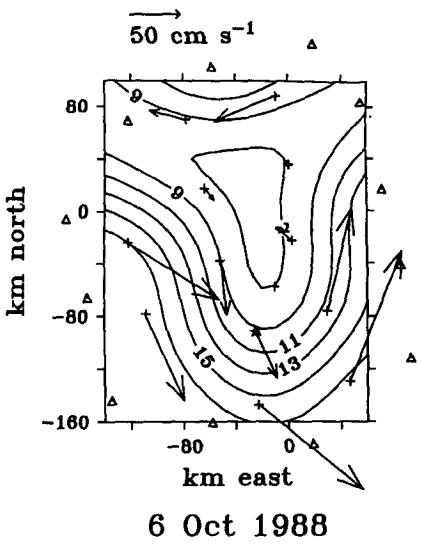

FIG. 2. An example of a large amplitude meander that formed in the study region. The contoured field is temperature at 400 m for 6 Oct 1988. Temperature was measured at all mooring sites shown. In addition, temperature at 400 m was estimated from IES at locations marked with triangles. The vectors are the 400-m-level geostrophic velocities for 6 Oct 1988. The mapped region is the boxed region shown in Fig. 1.

The Marshall and Shutts decomposition

The temperature variance maps can be used to estimate the nondivergent heat flux according to the MS decomposition (8)–(9):

$$\overline{\mathbf{u}'T'}^{\text{nondiv}} = \frac{d\bar{\psi}}{d\bar{T}}\hat{\mathbf{z}} \times \nabla \frac{1}{2}\overline{T'^2}$$

$$\overline{\mathbf{u}'T'}^{\text{div}} = \overline{\mathbf{u}'T'} - \overline{\mathbf{u}'T'}^{\text{nondiv}},$$

where $d\bar{\psi}/d\bar{T}$ is an empirical factor estimated from the data. Figure 4a shows the mean streamlines superimposed on the mean temperature contours. To estimate the factor $d\bar{\psi}/d\bar{T}$, for each level a line was fitted to the scatterplot of $\bar{\psi}$ and $\bar{T}$ values from the low-error region of the mapped fields. These scatterplots are shown in Fig. 4b. The relation between $\bar{T}$ and $\bar{\psi}$ turns out to be linear throughout nearly the entire temperature range (which is not required, but simplifies the treatment).

Figure 5a shows the heat fluxes superimposed on the temperature variance maps; Fig. 5b shows the divergent and nondivergent heat fluxes again superimposed on the temperature variance maps. Notice that the nondivergent heat fluxes are always tangent to the temperature variance contours. Because there is a local maximum in the temperature variance field associated with the trough axis, the nondivergent heat fluxes are oriented northward upstream of the trough axis and southward downstream of the trough axis.

5. Evaluation of the eddy energy budgets at 68°W

The data are well suited for evaluating the eddy energy budgets [(6) and (12)]. The observational array was specifically designed to measure the mass and flow fields with sufficient resolution and duration to evaluate and map the mean fields ($\bar{u}$, $\bar{v}$, $\bar{T}$) and flux fields ($\overline{u'u'}$, $\overline{u'v'}$, $\overline{v'v'}$, $\overline{u'T'}$, $\overline{v'T'}$). Central finite differences with $2\Delta x$, $2\Delta y$ of 40 km have been used to evaluate the gradients of the mapped (gridded) fields.

The factors g, α, and θ_z have been determined from independent sources: g the acceleration due to gravity has been approximated by 980 cm s^{-2}; α the effective thermal expansion coefficient has been calculated to be 1.0×10^{-4} °C^{-1} for the temperature ranges 2.2°–3.6°C (approximately 3500 m) and 5°–17.5°C (approximately 400–1000 m) using the methodology of Bryden (1982) on NODC CTD data of the Gulf Stream region;

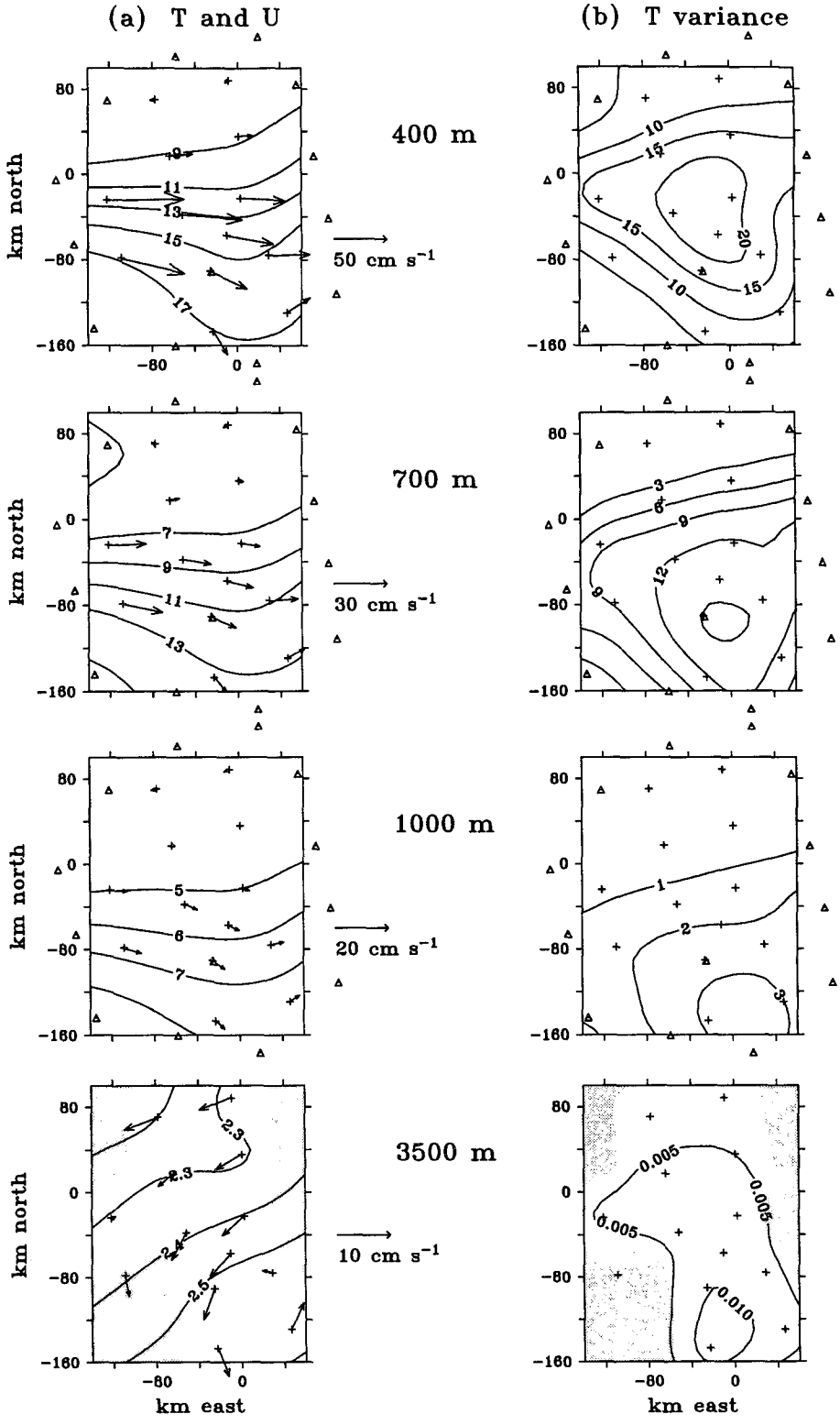

FIG. 3. (a) (left column) Mean temperature fields with mean velocity vectors superimposed at 400, 700, 1000, and 3500 m. (b) (right column) Temperature variance maps at the four levels. Plus marks indicate mooring sites that had temperature and velocity measurements. Triangles indicate IES sites used to estimate temperature at 400–1000 m. In the light shaded regions, the temperature error variance is greater than 50% of the expected variance.

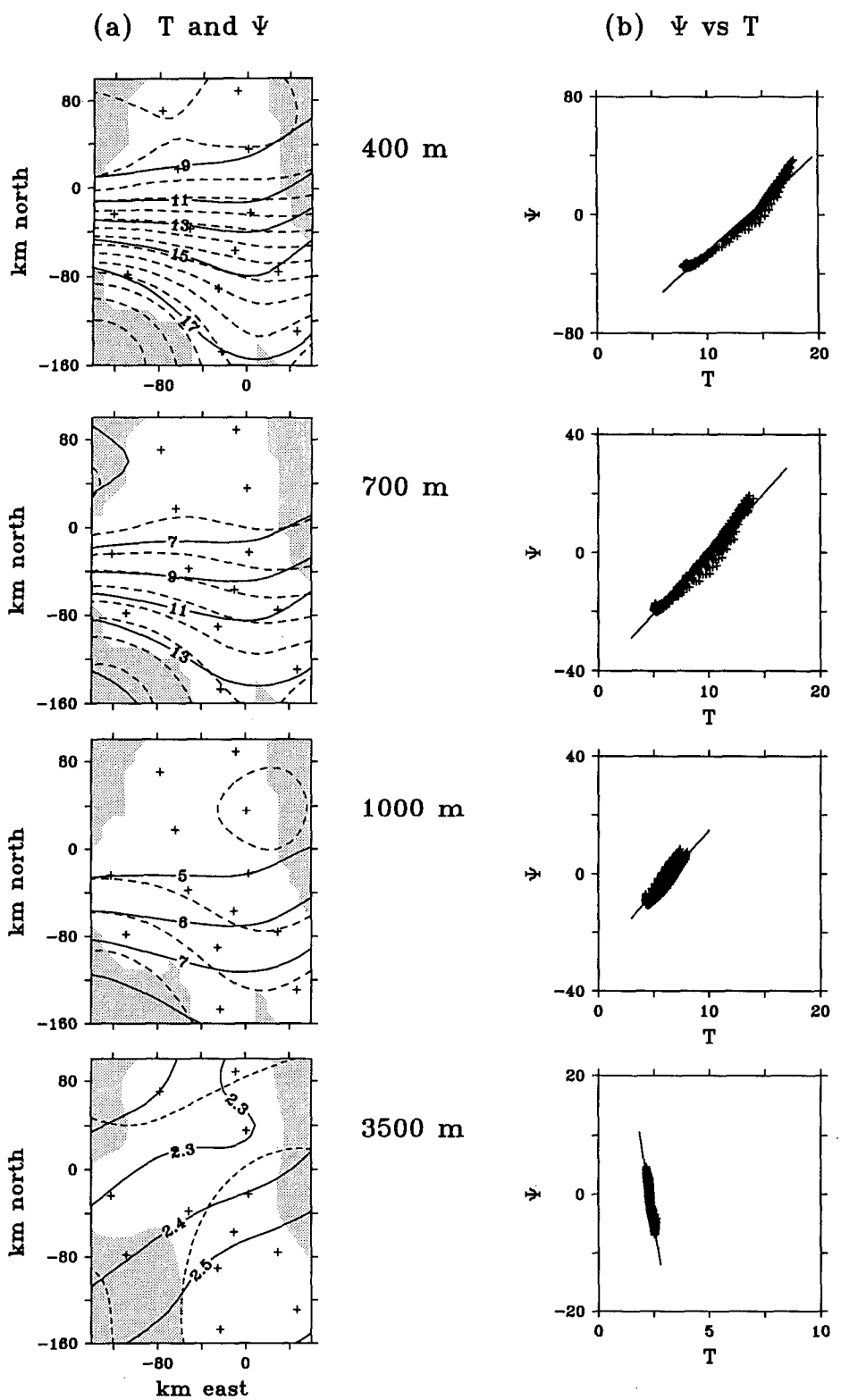

FIG. 4. (a) (left column) Maps of the mean temperature (solid) and mean streamlines (dashed). Light shaded regions have normalized velocity error variance greater than 50%; dark shaded regions have normalized error variance greater than 100%. Only data from regions with error less than 50% were used in the regression to find $d\bar{\psi}/d\bar{T}$. (b) (right column) The scatterplots of the mean temperature and mean streamfunction from the low-error region shown in (a). The straight line was estimated by linear regression.

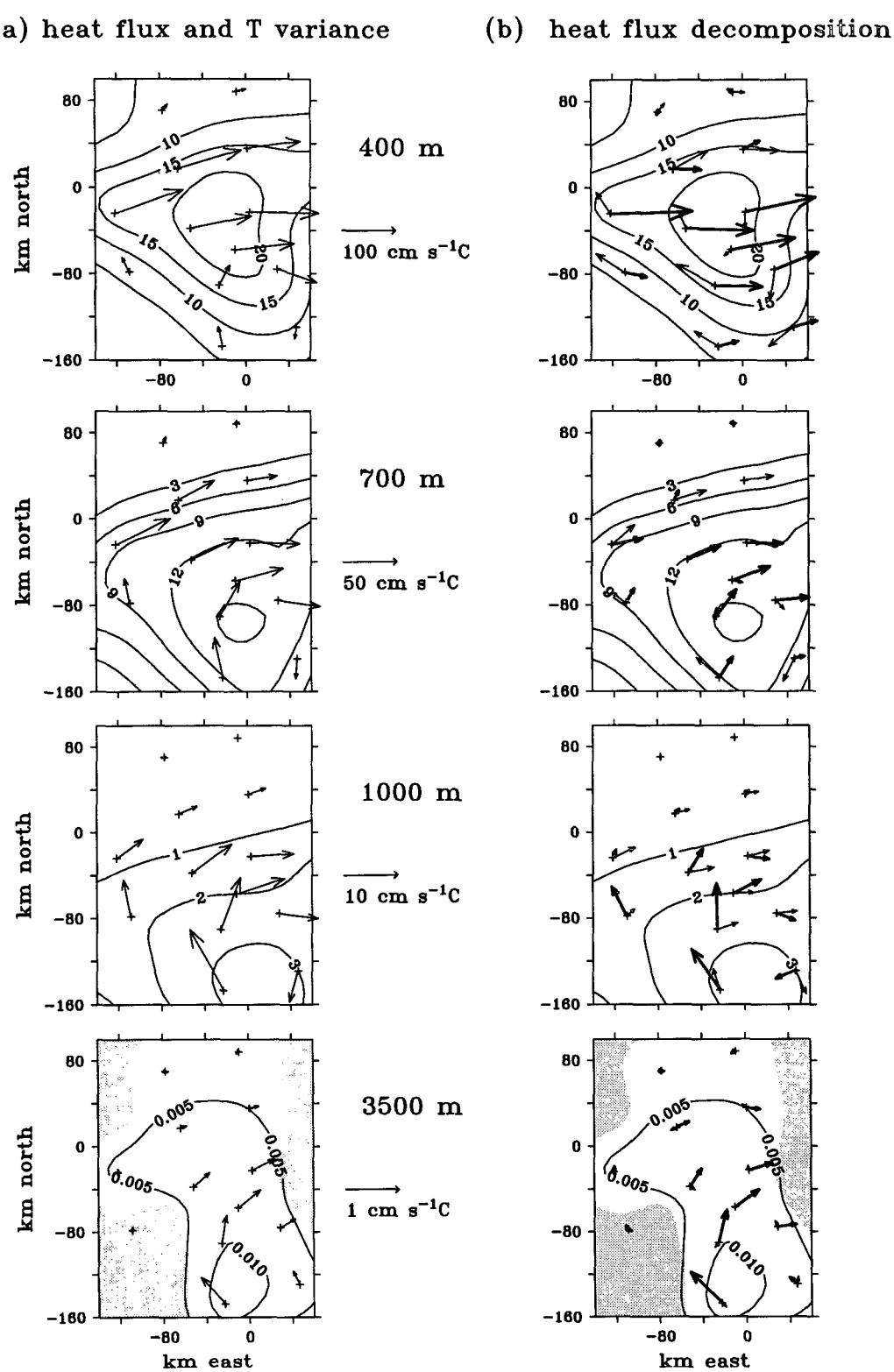

FIG. 5. (a) (left column) Heat flux vectors superimposed on maps of the temperature variance field. (b) (right column) The nondivergent (light) and residual divergent (dark) heat flux components superimposed on the temperature variance field. The nondivergent heat flux vectors, estimated using the Marshall and Shutts method, are always tangent to temperature variance contours. Together, the divergent and nondivergent components sum to be the total vector field shown in (a).

and θ_z has been estimated from the mean Pegasus cross section at 73°W (Halkin et al. 1985) to be approximately 1°C/60 m (1.7×10^{-4} °C cm^{-1}) for the 400-m and 700-m levels, 1°C/100 m (1.0×10^{-4} °C cm^{-1}) for the 1000-m level, and 1°C/1000 m (1.0×10^{-5} °C cm^{-1}) for the 3500-m level. Thus, the factor $g\alpha/\theta_z$ is only a function of depth in our study region; for a given level, the EPE maps are proportional to the temperature variance maps.

In the following figures, all fields are sufficiently depth dependent that the contour interval must decrease with each deeper level. The units of all energy transfer rate contours are 10^{-3} cm^{-2} s^{-3}. As discussed in appendix B, the OI output fields (u, v, T, ψ) are lightly shaded when the percent error variance is larger than 50% and darkly shaded when the error variance is larger than 100% and the sign would not be significant.

a. Mean advection of EPE (MAP)

Figure 6a shows the mean velocity vectors $\bar{\mathbf{u}}$ superimposed on the temperature variance $\overline{T'^2}$ fields (which are proportional to the EPE = $g\alpha/2\theta_z\overline{T'^2}$ fields), and Fig. 6b shows the mapped mean advection of EPE: MAP = $-\bar{\mathbf{u}}\cdot\nabla$EPE. West of the trough axis, there is a mean advection of low EPE; while east of the trough axis, there is evidence of mean advection of high EPE. The maximum (negative) values are along the core of the mean jet and have central peak values exceeding -16×10^{-3} cm^{-2} s^{-3} at 400 m, -4×10^{-3} cm^{-2} s^{-3} at 700 m, and -1×10^{-3} cm^{-2} s^{-3} at 1000 m. Because of the baroclinicity of the mean jet, the jet axis is shifted southward with depth. A southward shift with depth in the mean advection of EPE is also evident, as can be seen in Fig. 6b.

In the deep layer at 3500 m, the mean velocity is predominantly westward due to the deep western boundary current. Thus, the pattern of mean EPE advection is opposite that found in the upper layer, having a positive value to the west of the trough axis and a negative value to the east.

b. Traditional baroclinic conversion rate (BC)

Figure 7a shows the horizontal eddy heat flux vectors $\overline{\mathbf{u}'T'}$ superimposed on the mean temperature contours $\bar{T}$, and Fig. 7b shows the mapped downgradient heat flux term (the traditional baroclinic conversion rate):

$$\mathrm{BC} = -\frac{g\alpha}{\theta_z}\overline{\mathbf{u}'T'}\cdot\nabla\bar{T}.$$

The heat flux vectors in Fig. 7a should not be confused with the mean flow vectors in Fig. 6a. To interpret Fig. 7a, note that if the mean temperature contours are zonal with colder temperatures to the north, then a downgradient heat flux will bring warm water northward or cold water southward. Therefore a downgradient heat flux will have a component that is northward of the mean temperature contour.

Although the mean temperature contours, shown in Fig. 7a, are nearly zonal in the upper layer, there is evidence of a trough in the southern portion of the array. In the deep layer, the temperature contours are oriented northeast–southwest, perhaps aligned with the bathymetry. As with the other energetic terms, the asymmetry relative to the trough axis is clearly evident: There appear to be downgradient heat fluxes at all the moorings upstream of the trough axis and upgradient heat fluxes downstream of it. The maximum (positive) values of BC are along the core of the mean jet and have approximate values of 16×10^{-3} cm^{-2} s^{-3} at 400 m, 12×10^{-3} cm^{-2} s^{-3} at 700 m, 2×10^{-3} cm^{-2} s^{-3} at 1000 m, and 0.04×10^{-3} cm^{-2} s^{-3} at 3500 m.

Comparing Fig. 7b with 6b, we see that at 400 m the downgradient heat fluxes tend to balance the downstream change in EPE. However, at 700 and 1000 m, the traditional BC terms are a factor of 2–3 times larger than the mean advection of EPE, suggesting that there could be conversions from MPE to EPE occurring at these levels.

c. Dynamical baroclinic conversion rate (dynBC)

Figure 8a shows the divergent heat fluxes $\overline{\mathbf{u}'T'}^{\mathrm{div}}$ superimposed on the mean temperature field $\bar{T}$, and Fig. 8b shows maps of the dynamical baroclinic conversion rate:

$$\mathrm{dynBC} = -\frac{g\alpha}{\theta_z}\overline{\mathbf{u}'T'}^{\mathrm{div}}\cdot\nabla\bar{T}.$$

Comparing Fig. 8a to 7a, we see that the largest qualitative differences between the divergent heat flux and the full heat flux occur away from the jet axis, where the flow is nearly equivalent barotropic and the divergent heat flux is small. Comparing Fig. 8b to 7b, we see that this MS decomposition has reduced the traditional rate of baroclinic conversion by nearly 60% at 400 m, 40% at 700 and 1000 m, and 30% at 3500 m. Although the mean trough axis is near the eastern edge of our measurement array, an asymmetry is still evident in the baroclinic conversion term relative to the trough axis.

d. Eddy advection of EPE (EAP)

Traditionally, the eddy advection of EPE [EAP = $-\nabla\cdot(g\alpha/2\theta_z)\mathbf{u}'T'^2$] is ignored. Certainly, being a triple correlation, its statistical significance is worse than the other terms. However, as can be seen from the masking in Fig. 9, this term stands well above its measurement error. Furthermore, values of EAP are of similar magnitude to the MAP and BC terms, although the pattern appears to be aligned with the jet axis rather than the trough axis. To the north of the jet axis, EAP is negative; to the south of the jet axis, EAP is positive.

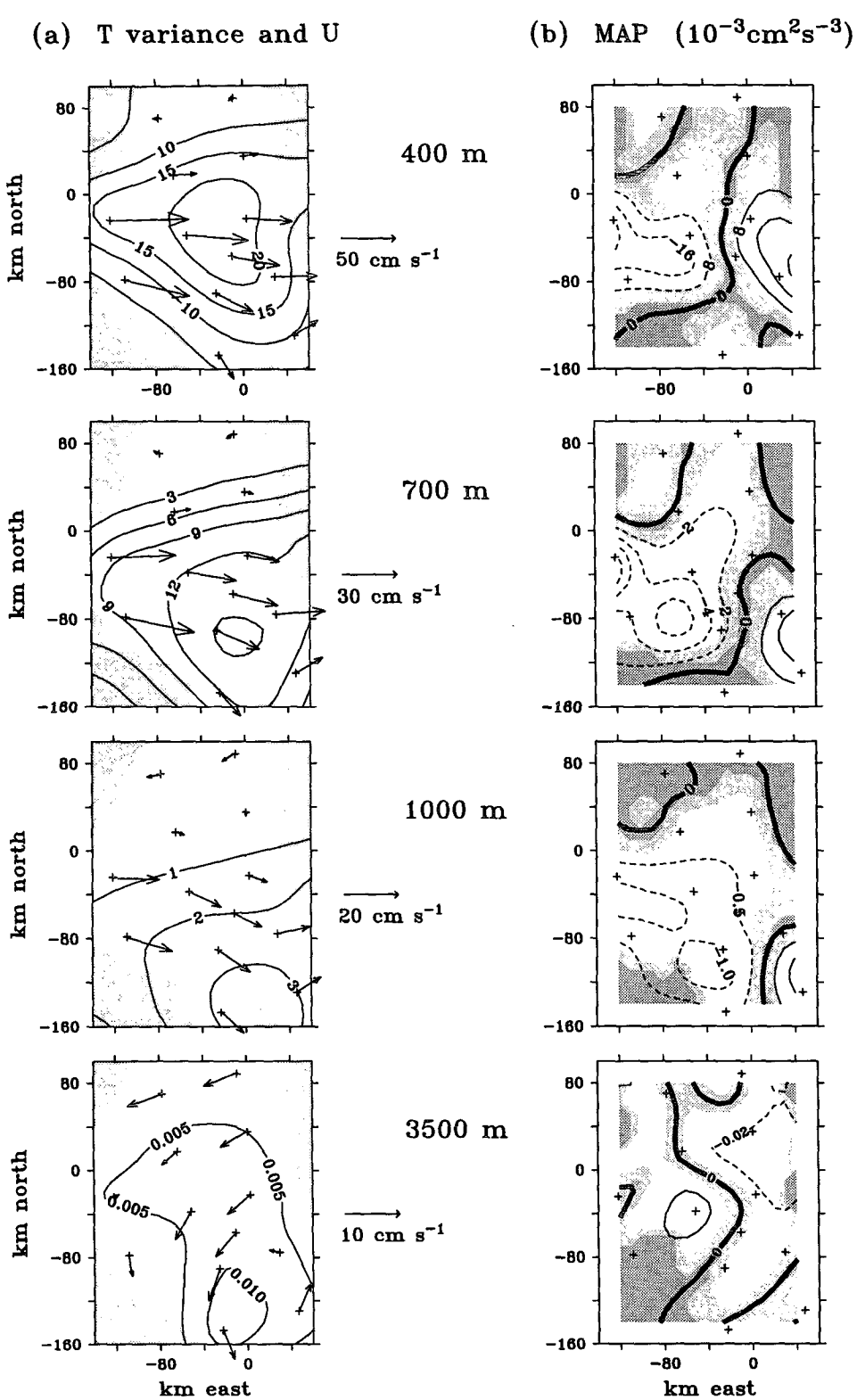

FIG. 6. (a) (left column) Temperature variance fields with mean velocity vectors for 400, 700, 1000, and 3500 m. (b) (right column) The mean advection of EPE (MAP). The CI of the energetic terms in Figs. 6b, 7b, 8b, 9, and 10 are 8×10^{-3} cm^2 s^{-3}, 2×10^{-3} cm^2 s^{-3}, 0.5×10^{-3} cm^2 s^{-3}, and 0.02×10^{-3} cm^2 s^{-3} for the levels 400, 700, 1000, and 3500 m. As discussed in appendix B, the light shaded regions in these figures have errors of greater than 50% of the computed term, and the dark shaded regions have errors larger than the computed energetic term.

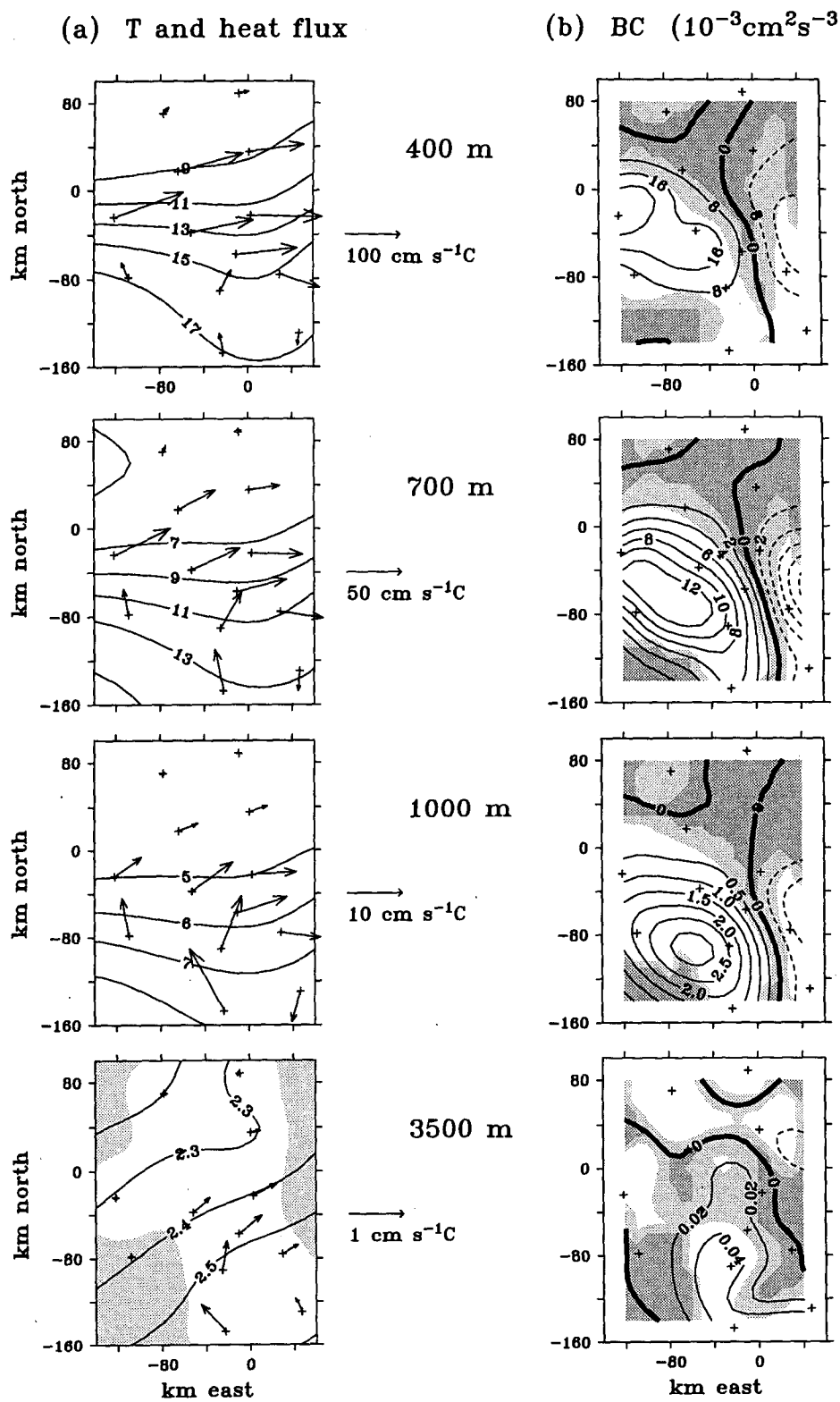

FIG. 7. (a) (left column) Heat flux vectors superimposed on the mean temperature contours. (b) (right column) The traditional baroclinic conversion rate (BC). Units, CI, and shading convention are explained in Fig. 6.

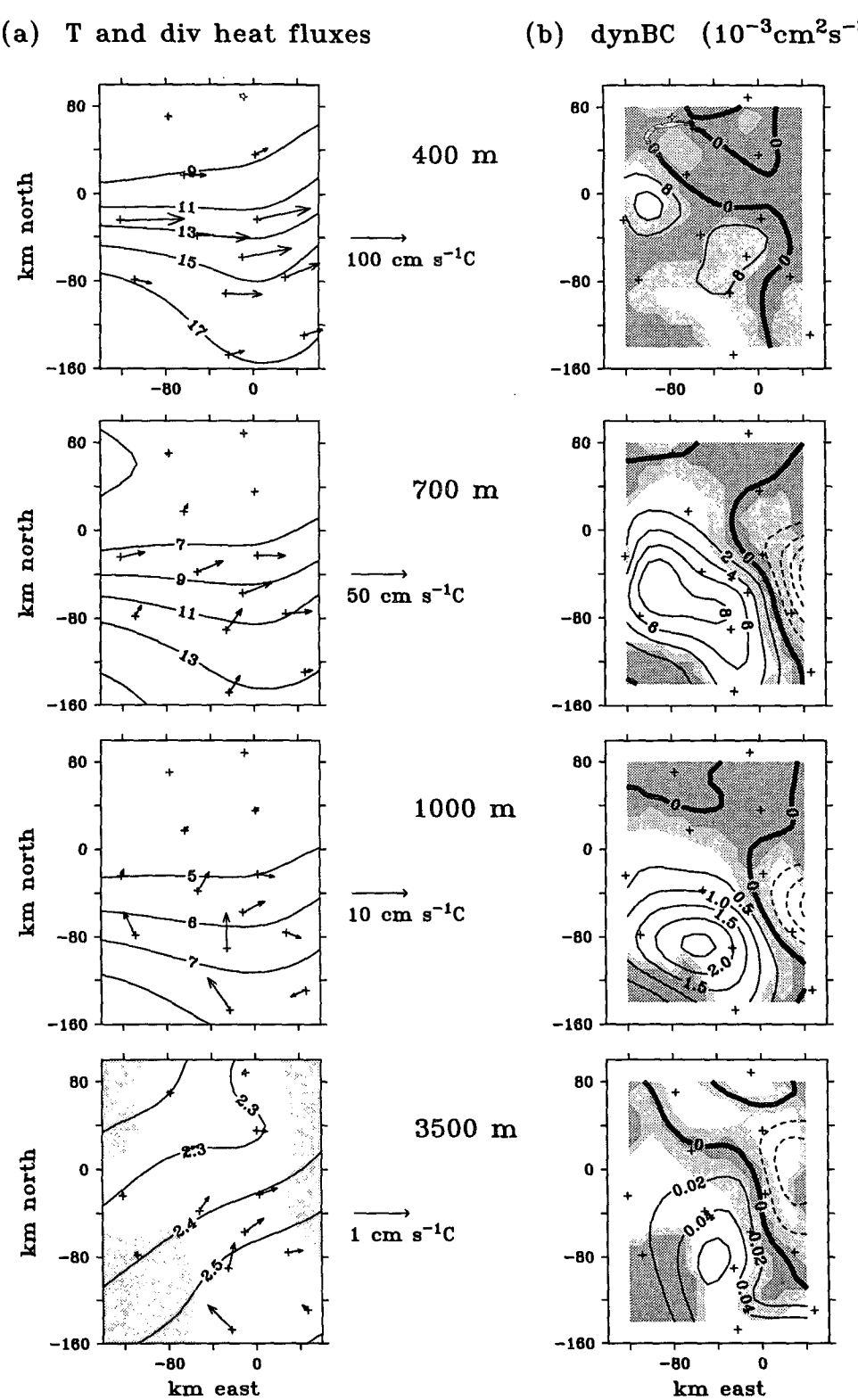

FIG. 8. (a) (left column) Divergent eddy heat flux vectors superimposed on maps of the mean temperature field. (b) (right column) The dynamical rate of baroclinic conversion calculated using the downgradient divergent eddy heat flux (dynBC). Units, CI, and shading convention are explained in Fig. 6.

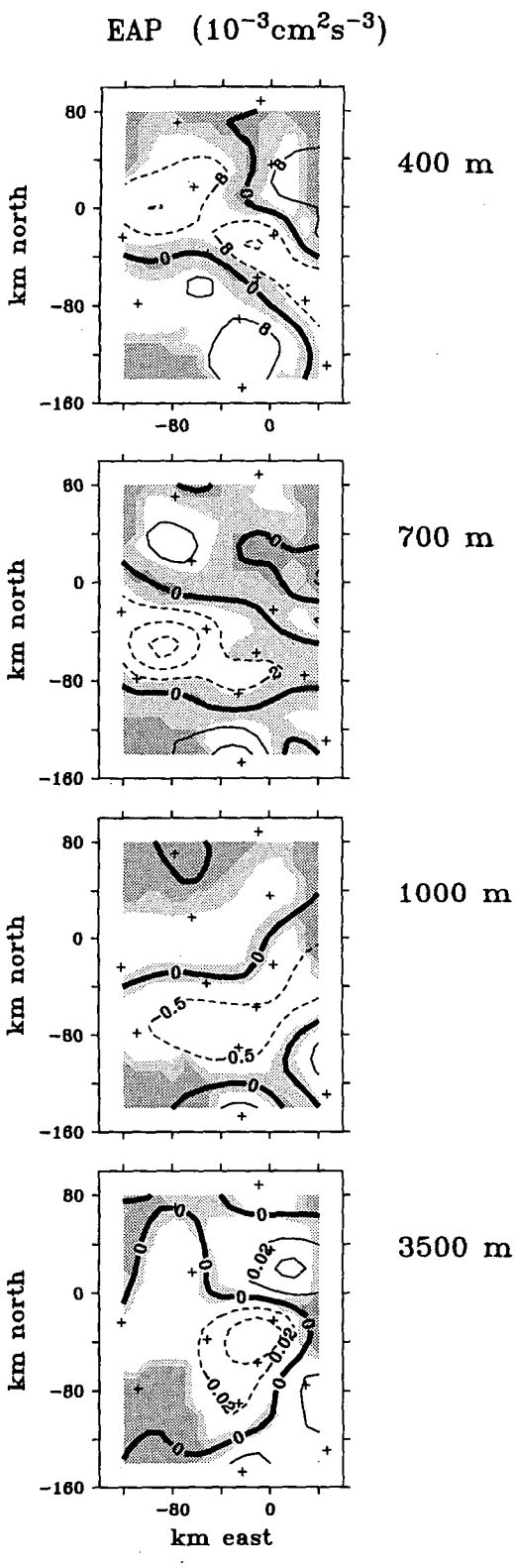

FIG. 9. Eddy advection of EPE (EAP) at 400, 700, 1000, and 3500 m. Units, CI, and shading convention are explained in Fig. 6.

A southward shift with depth in the EAP pattern is also evident, perhaps due to the southward shift with depth in the jet axis. Maximum (negative) values of EAP are along the northern side of the mean jet axis and have approximate values of -8×10^{-3} cm^{-2} s^{-3} at 400 m, -4×10^{-3} cm^{-2} s^{-3} at 700 m, -0.5×10^{-3} cm^{-2} s^{-3} at 1000 m, and -0.04×10^{-3} cm^{-2} s^{-3} at 3500 m.

e. Residual rate of conversion of EPE to EKE (PKC)

Figure 10 shows the sum of the MAP + BC + EAP terms that constitute the residual rate of conversion from EPE to EKE (PKC = $g\alpha\overline{w'T'}$). Positive contours of this term correspond to bringing warm water upward or cold water downward (i.e., upgradient).

At all levels in the region just upstream of the trough axis and south of the jet axis, the vertical eddy heat fluxes are generally upgradient, producing a conversion of EPE to EKE. The maximum PKC conversion rates are 16×10^{-3} cm^{-2} s^{-3} at 400 m, 12×10^{-3} cm^{-2} s^{-3} at 700 m, 1.5×10^{-3} cm^{-2} s^{-3} at 1000 m, and 0.04×10^{-3} cm^{-2} s^{-3} at 3500 m.

f. Barotropic conversion rate (BT)

Figure 11a shows the velocity variance ellipses (Fofonoff 1969) superimposed on the mean streamlines for each level, and Fig. 11b shows the mapped barotropic conversion rate

$$\mathrm{BT} = -\left[\overline{u'u'}\frac{\partial \bar{u}}{\partial x} + \overline{u'v'}\left(\frac{\partial \bar{u}}{\partial y} + \frac{\partial \bar{v}}{\partial x}\right) + \overline{v'v'}\frac{\partial \bar{v}}{\partial y}\right].$$

The variance ellipses show the degree and direction of anisotropy. A perfectly round variance ellipse indicates random fluctuations in all directions ($\overline{u'u'} = \overline{v'v'}$ and $\overline{u'v'} = 0$); a line variance ellipse directed at 45° indicates that the u and v fluctuations are perfectly correlated. Thus, elongated variance ellipses that lean against the shear produce downgradient momentum fluxes (positive contours in Fig. 11b).

Although the errors are as large as the signal throughout much of the study region, the barotropic conversion terms have an apparent double lobed pattern with a positive maximum (i.e., increasing the EKE) along the cyclonic and anticyclonic sides of the mean jet. The maximum values occur on the cyclonic side and have approximate values of 4×10^{-3} cm^{-2} s^{-3} at 400 m, 1×10^{-3} cm^{-2} s^{-3} at 700 m, 0.1×10^{-3} cm^{-2} s^{-3} at 1000 m, and 0.01×10^{-3} cm^{-2} s^{-3} at 3500 m.

Comparing the rate of barotropic conversion (Fig. 11b) to the dynamical baroclinic conversion rate (Fig. 8b), we see that at 400 m the dynamical baroclinic conversion rate is approximately 1.5 times larger than the barotropic rate, while at 700 m and 1000 m the baroclinic conversion rate is respectively 7 times and 13 times larger than the corresponding rate of barotropic conversion. At 3500 m, the large measurement errors make the comparison difficult; however, it ap-

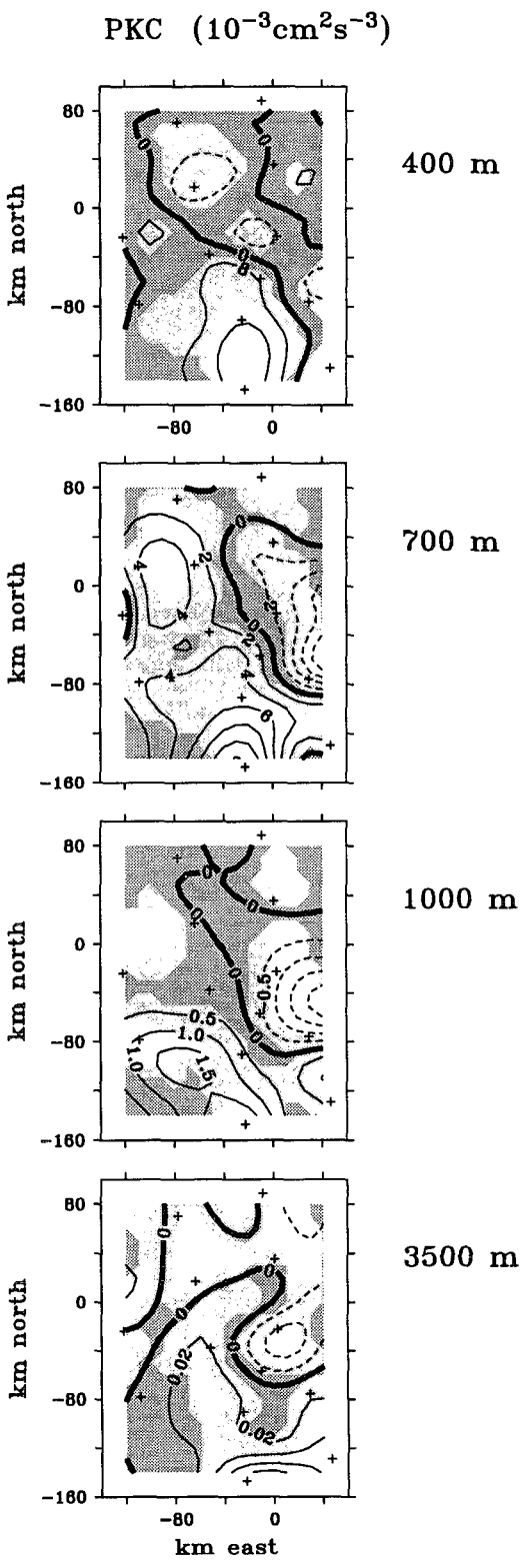

FIG. 10. The residual rate of conversion from EPE to EKE (PKC). The units are the same as in all energetic transfer rate maps. Units, CI, and shading convention are explained in Fig. 6.

pears that the baroclinic conversion term is still larger than the barotropic term, although both are approximately two orders of magnitude smaller than the conversion rates in the upper layer.

g. Mean advection of EKE (MAK)

Figure 12a shows the mean velocity vectors $\bar{\mathbf{u}}$ superimposed on the EKE field; and Fig. 12b shows the mapped rate of mean advection of EKE: MAK $= -\bar{\mathbf{u}}\cdot\nabla$EKE. Notice that in the upper levels, the rate of mean advection of EKE has maximum values along the core of the jet in the western portion of the array. However, there is some evidence that there is a change of sign east of the "trough axis." This pattern is evident at all three upper levels, although the maximum values are reduced significantly from -4×10^{-3} cm^{-2} s^{-3} at 400 m, to -0.5×10^{-3} cm^{-2} s^{-3} at 700 m, to -0.1×10^{-3} cm^{-2} s^{-3} at 1000 m.

In the deep level, the mean velocity vectors tend to rotate around the EKE contours, and therefore the deep mean EKE advection is negligible.

h. Eddy advection of EKE (EAK)

The eddy advection of EKE: EAK $= -\nabla\cdot\overline{\mathbf{u}'\mathrm{EKE}'}$ is shown in Fig. 13. Like the eddy and mean advections of EPE, the eddy advection of EKE is often as large as the mean advection of the EKE (where, recall, a positive mean advection is equivalent to a negative downstream change). In the deep layer, the eddy advection of EKE is a dominant term in the eddy energy budget and is probably balanced by the (unmeasured) horizontal eddy pressure work term.

6. Summary of energetics analysis at 68°W

Traditionally, these energy transfer rates are summarized in a Lorenz box diagram in which MPE, MKE, EPE, and EKE are represented as four boxes and sources and sinks of these energies are represented as arrows into and out of the given box. Conversion rates are represented as arrows between the boxes. Figure 14 shows the Lorenz diagram, which characterizes our study region at 68°W upstream of the trough axis. The numbers listed for each arrow are the spatially averaged transfer rate for each of the four levels 400, 700, 1000, and 3500 m and their associated measurement error. The region used in the spatial average is the box upstream of the trough axis defined by -90 km $\leq x \leq -40$ km and -120 km $\leq y \leq 40$ km in the coordinate system shown in Figs. 2–13 (i.e., km east and north relative to 38°N and 68°W). Because this paper has focused on the eddy energy budget and the sources of eddy variance, only the sources and sinks of EKE and EPE have been listed in Fig. 14.

Although the traditional Lorenz diagram provides a graphical and easily remembered way of displaying the complicated coupled energy budgets, there are two

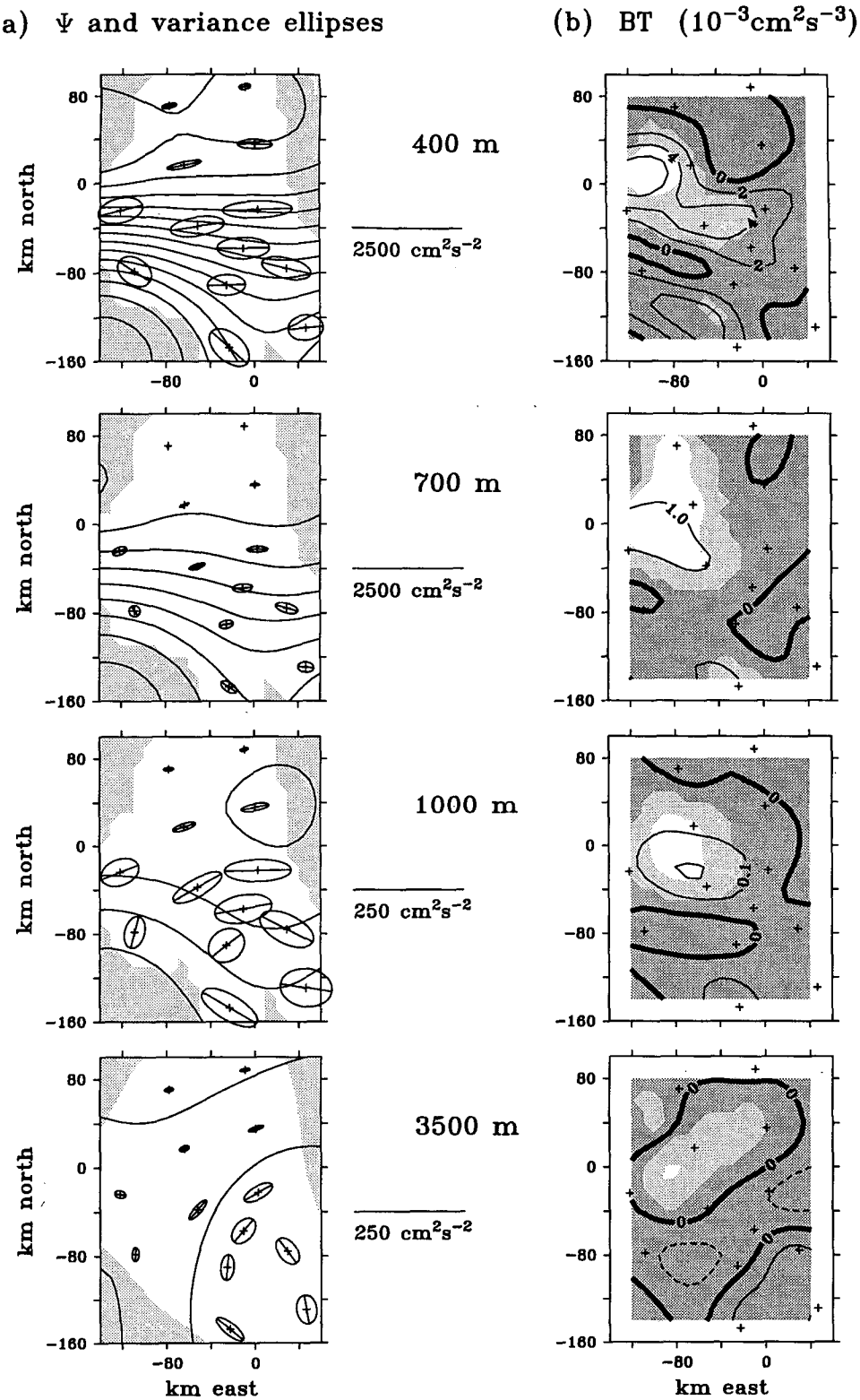

FIG. 11. (a) (left column) Variance ellipses of the perturbation flow evaluated at the mooring sites superimposed on maps of the mean streamlines. (b) (right column) The rate of barotropic conversion from MKE to EKE (BT). The CI of the energetic terms in Figs. 11b, 12b, and 13 are 2×10^{-3} cm^2 s^{-3}, 1×10^{-3} cm^2 s^{-3}, 0.1×10^{-3} cm^2 s^{-3}, and 0.02×10^{-3} cm^2 s^{-3} for levels 400, 700, 1000, and 3500 m.

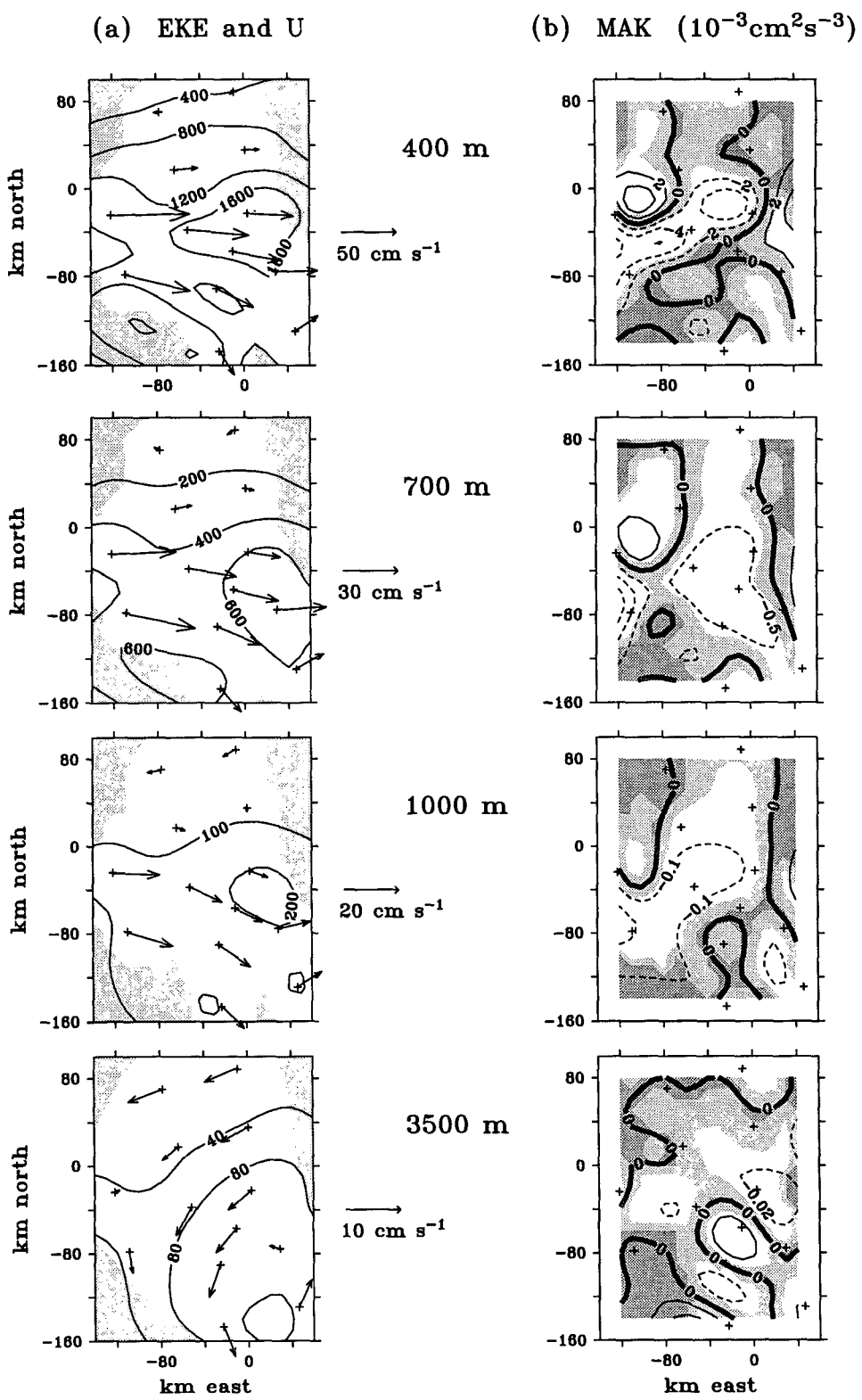

FIG. 12. (a) (left column) The mean flow vectors superimposed on maps of the eddy kinetic energy. (b) (right column) Mean advection of EKE (MAK). Units, CI, and shading convention are explained in Fig. 11.

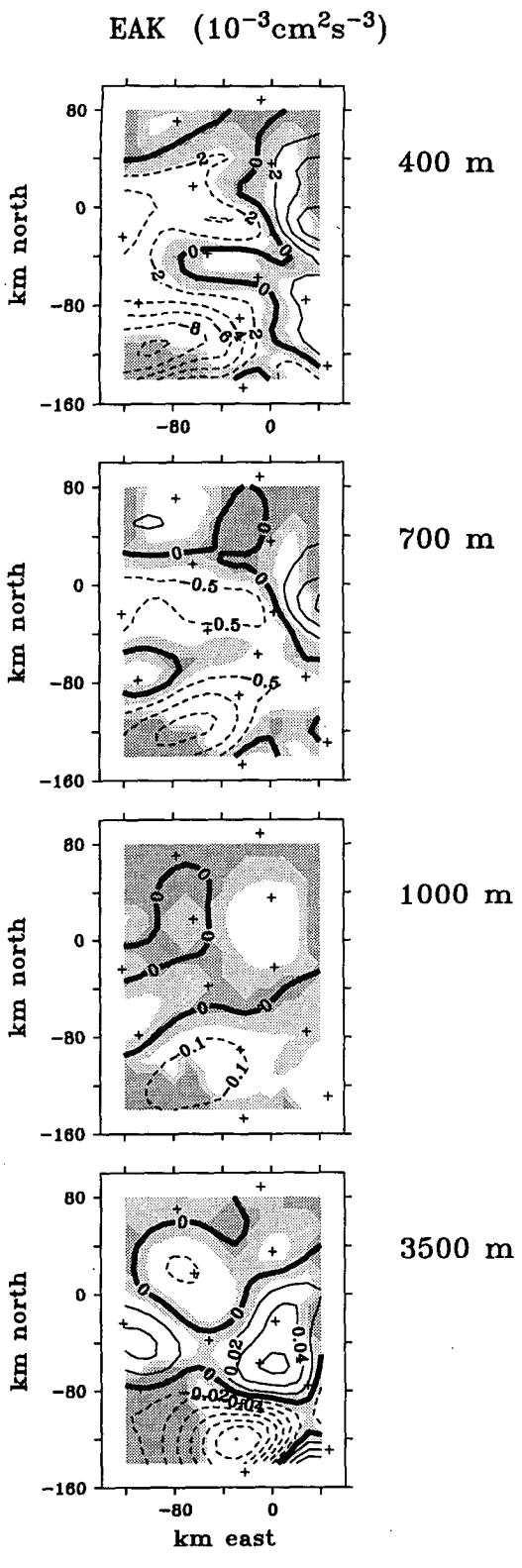

FIG. 13. Eddy advection of EKE (EAK) at 400, 700, 1000, and 3500 m. Units, CI, and shading convention are explained in Fig. 11.

problems with this type of box diagram, which we will address here. First, no distinction is made between the divergent and nondivergent eddy fluxes. The downgradient *non*divergent heat flux term (traditionally considered a portion of the rate of baroclinic conversion of MPE to EPE) can be nonzero even under conditions in which there is no conversion process occurring and identically balances a portion of the mean EPE advection.

The second problem with the traditional Lorenz diagram is that the pressure work term is represented as an independent source (or sink) of kinetic energy. This is misleading since the fluid is in hydrostatic balance and the vertical heat fluxes (the EPE to EKE conversion rate) are identically equal to the vertical eddy pressure work. The mass (EPE) and flow (EKE) fields are coupled via the pressure work terms.

Thus, the Lorenz diagram can be further modified to make the coupling of the potential and kinetic energies via pressure work explicit. As in the traditional Lorenz diagrams, each energy budget is represented as a box with arrows into and out of the energy box representing the sources and sinks of the energy. However, in the modified Lorenz diagram, the EPE and EKE boxes are connected by arrows that must go through a circled (as opposed to boxed) P'/ρ_0. The use of circles and boxes is meant to highlight the distinction between budgets (boxes) and terms that couple the budgets (circles) but are not conversion rates. The arrow between the boxed EPE and the circled P'/ρ_0 is the vertical eddy heat flux (the traditional EPE to EKE conversion rate), which by the hydrostatic relation is identically equal to the vertical eddy pressure work. The horizontal eddy pressure work term is represented as an arrow between the circled P'/ρ_0 and the boxed EKE. Note that the horizontal and vertical eddy pressure work need not be equal. The MPE and MKE budgets are similarly coupled via mean pressure work.

At all four levels, but particularly at 400 m, the BC and MAP terms tend to offset each other due to the nondivergent heat fluxes. The dynamical baroclinic conversion rate dynBC takes into account this partial cancellation and is nearly 50% less than the traditional BC value, as shown in Fig. 15. Nevertheless, dynBC is still larger than the barotropic conversion rate BT by an approximate factor of 7 in the upper layer. Thus, the mean potential energy appears to be the dominant source of eddy energy in this region.

For much of the array, the redistribution of the mass field due to the effects of the mean and eddy advection of EPE and the horizontal downgradient heat fluxes results in a vertical upgradient heat flux. Because the divergent horizontal heat fluxes are downgradient and the vertical heat fluxes are upgradient, the dynamical heat flux vectors are oriented within the "wedge of instability," that is, above the horizontal but below the time-averaged sloped temperature front (Pedlosky

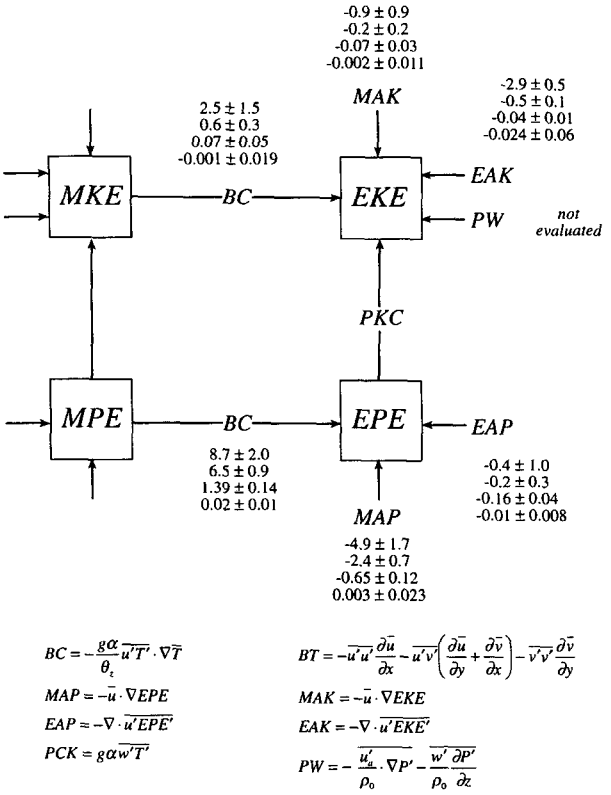

FIG. 14. The traditional Lorenz diagram. Boxes represent budgets. Arrows into (out of) a box represent sources (sinks) of the energy. Arrows between boxes represent conversions. The listed transfer rates and associated measurement error (see text) for each level (400, 700, 1000, and 3500 m) are average values within the box upstream of the trough axis defined by -90 km $\leq x \leq -40$ km and -120 km $\leq y \leq 40$ km in the coordinate system of Figs. 2–13 (i.e., relative to 38°N and 68°W). The units for all values are 10^{-3} cm^2 s^{-3}.

1987). The heat fluxes are thus indicative of a baroclinically unstable mean jet.

By the hydrostatic relation, the vertical heat flux is identically balanced by a negative vertical pressure work term:

$$g\alpha\overline{w'T'} = \overline{w'\frac{\partial}{\partial z}\frac{P'}{\rho_0}},$$

which acts as a source of EKE. If this eddy kinetic energy source $g\alpha\overline{w'T'}$ has horizontal gradients (as it does at 400 m), then the horizontal distribution of the vertical pressure work will induce horizontal ageostrophic pressure work terms, which in turn must be balanced by either eddy advection of EKE or a downstream change in EKE. To a certain extent this appears to be happening at 400 m; while at 700 m and 1000 m, the vertical heat flux is more uniformly upgradient (positive PKC see Fig. 10) and there are only weak downstream changes in the EKE field.

7. Discussion

This study was designed to measure the three-dimensional structure of the energy transfer rates. The structure of the barotropic conversion rate has been particularly controversial in the past. Rossby (1987), using 19 Pegasus (density, velocity, pressure) cross sections at 73°W, created a vertical cross section of the barotropic conversion rate, which showed a double lobed pattern extending to 800 m, centered along the jet axis, with maximum values of the lobes roughly at 250-m depth. It should be noted that terms involving downstream gradients could not be estimated with this data. As can be seen in Fig. 11a, these neglected terms can sometimes be large.

While Rossby (1987) saw positive conversion rates on both sides of the stream, Hall (1986), using a single mooring at 68°W and defining the jet axis to be 13°C isotherm at 575 m, observed positive rates on the an-

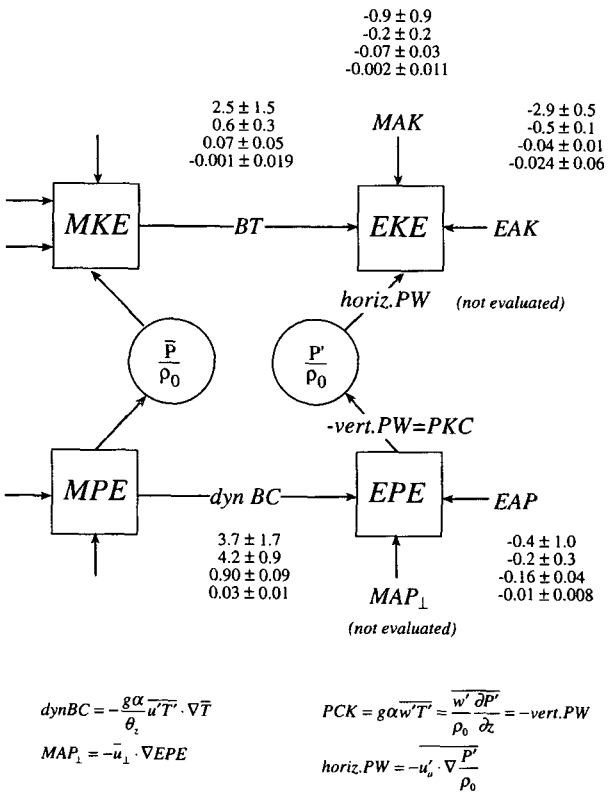

FIG. 15. The modified Lorenz diagram. The traditional Lorenz diagram has been modified to show that the potential and kinetic energies are coupled via pressure work and to remove the internal canceling between the downgradient nondivergent eddy heat flux and the mean advection of EPE. As in Fig. 14, boxes represent budgets and arrows into a box represent sources of the energy. The circled P'/ρ is not a budget and the rates of horizontal and vertical eddy pressure work need not balance. Average values and associated measurement error for each level (400, 700, 1000, and 3500 m) are listed with units of 10^{-3} cm^2 s^{-3}. BT, MAK, EAK, and EAP are defined in Fig. 14.

ticyclonic side and weakly negative rates on the cyclonic side. In contrast, Kontoyiannis (1996), using a quasigeostrophic mixed baroclinic/barotropic instability channel model of the Gulf Stream at 73°W, created a cross section of the zonally averaged barotropic conversion rate, which had a double lobed pattern with positive values on the cyclonic side and weakly negative values on the anticyclonic side. Our maps of the barotropic conversion rate at 400 m, 700 m, 1000 m, and 3500 m are consistent with Rossby (1987), showing a double lobed pattern with positive rates on either side of the jet axis; however, the significance of the sign of the lobe on the anticyclonic side is questionable.

The values of the traditional baroclinic and barotropic conversion rates are remarkably similar to those found at 73°W by Rossby (1987) and Dewar and Bane (1989). Dewar and Bane (1989), using a cluster of moorings on the anticyclonic side of the stream, were able to estimate all terms in the traditional eddy energy budget at a single location. These studies, however, did not estimate the divergent heat fluxes. Therefore, it is difficult to know if their large baroclinic conversion rate was due to the nondivergent component or to the dynamically important divergent heat flux component.

The variance in the Gulf Stream at 68°W is inherently related to the prevalence of trough formation events in this region. A permanent trough feature is evident in the time-mean temperature and mean streamline fields and a local maximum in the temperature variance field occurs along the trough axis of the mean flow field. Although we have estimated the measurement errors rather than statistical errors, that the permanent trough feature at 68°W has been observed in the 93-month SST time series from satellite IR images (Lee 1994) suggests that our observations and budgets may characterize the long-term mean.

Figure 16 shows several events that contribute to the large downgradient horizontally divergent heat flux upstream of the trough axis: three trough formation events, a trough event that is in the process of pinching off to form a cold-core ring, and a crest amplification event. In all the events shown, the deep flow at 3500 m has speeds comparable in magnitude to the speeds at 700 m. In the trough formation events, the deep flow forms a cyclone whose center is downstream of the upper level trough axis. While in the crest amplification event, the deep flow forms a weak anticyclone whose center is downstream of the upper-level crest. This westward tilt with height in the streamlines is characteristic of baroclinic instability, whereby the trough and crest increase in amplitude due to geostrophic heat advection: Upstream of the trough the tilt produces a cyclonic turning with height (backing) and cold advection, which intensifies the upper-level trough, and upstream of the crest the westward tilt with height in the streamlines produces anticyclonic turning with height (veering) and warm advection, which intensifies the crest.

As discussed by Lindstrom and Watts (1994), if the pattern is stalled, as is the case with all six trough formation events, then the horizontal heat advection must be balanced by a vertical heat advection. Thus, in the trough events, the warm advection downstream of the trough is associated with upward motion of the water parcels. Essentially, between the trough and the crest the water parcels slide onshore and upward along sloped isopycnals (Bower and Rossby 1989). This vertical motion induces vertical stretching in the deep layer, which spins up the deep cyclone, and can further intensify the instability by intensifying the cold and warm advection.

In the statistical sense, baroclinic instability converts mean potential energy into eddy kinetic energy via eddy heat fluxes that are oriented in the "wedge of instability," that is, above the horizontal but below the time-averaged sloped temperature front (Pedlosky 1987). Thus, traditionally, a downgradient eddy heat flux is used as a signature of a baroclinic conversion process. However, it is possible to have an apparent baroclinic conversion arising from purely nondivergent heat fluxes, even when no heat advection occurs. As can be seen at 400 m (Figs. 6–7), much of the downgradient eddy heat flux is then balanced by the mean advection of EPE.

Because horizontally divergent heat fluxes are signatures of heat advection events, a downgradient horizontally divergent heat flux is an unambiguous signature of a baroclinic conversion process (i.e., a heat advection process that changes the center of mass of the fluid). This "dynamical" baroclinic conversion rate was evaluated from our mapped temperature and velocity fields using the Marshall and Shutts (1981) method, and even this reduced rate was still found to be at 700 m 7 times, and at 1000 m 13 times, larger than the barotropic conversion rate. This downgradient horizontally divergent heat flux, together with the upgradient vertical heat flux inferred from the traditional analysis, shows that the dynamical heat fluxes at 68°W are oriented in the wedge of instability. The eddy field and, in particular, the large troughs that form at 68°W are therefore caused by a true baroclinic conversion process. We conclude that the mean jet is baroclinically unstable at 68°W.

Acknowledgments. This work was supported by the NSF Grant OCE87-17144 and ONR Contracts N00014-90-J-1568, N00014-90-J-1548, and N00014-92-J-4013. Final revisions were made while MC was at NOAA/PMEL, funded by a NOAA postdoctoral fellowship in Climate and Global Change. The authors wish to thank Yuguang He for calculating the effective thermal expansion coefficient from historical data, Tom Shay for processing the current meter data, and Xiaoshu Qian and Nelson Hogg for their help and guidance in creating the gridded fields.

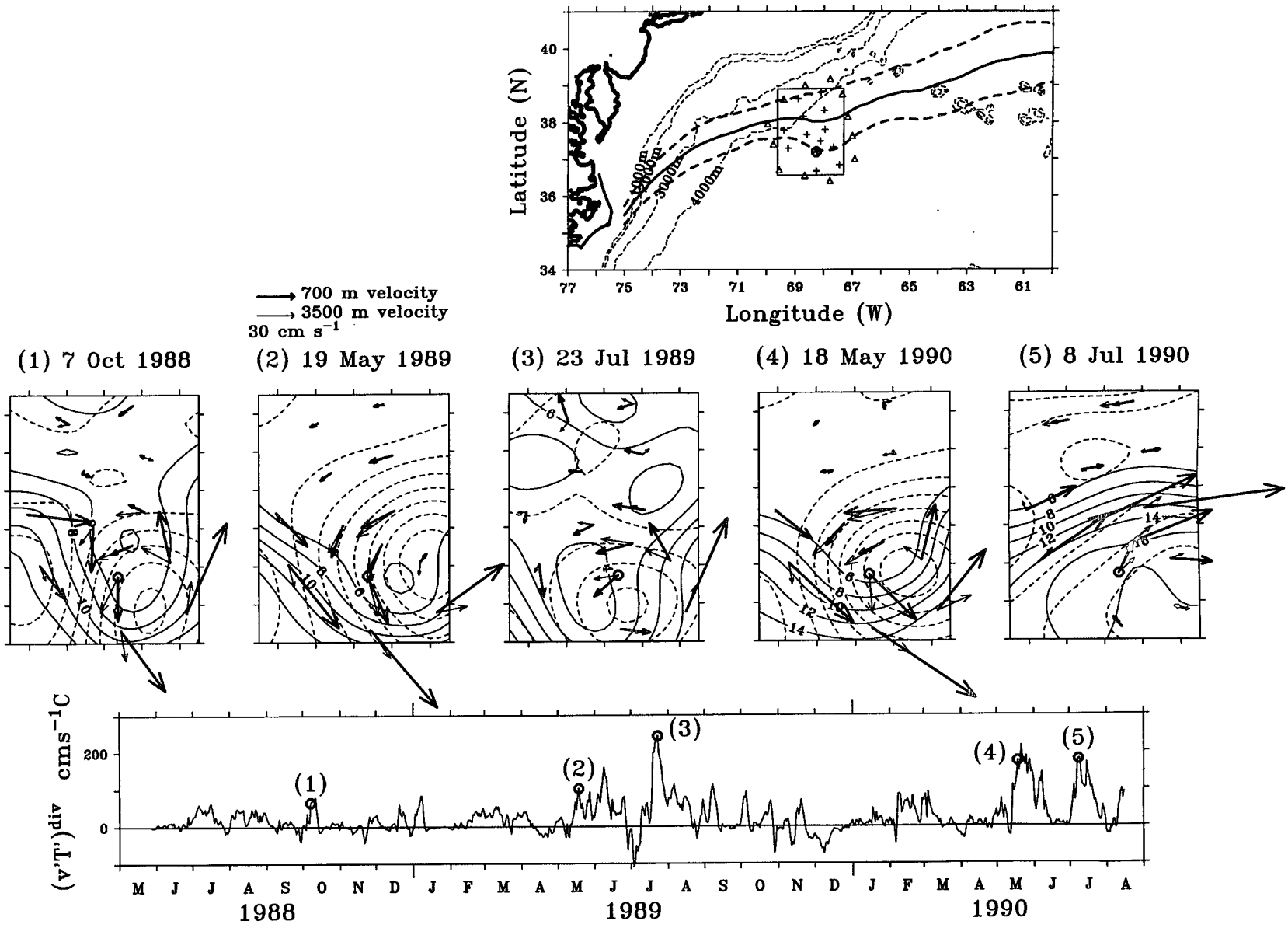

FIG. 16. The 700-m level $(v'T')^{div}$ time series at mooring site H5 (shown as an open circle in the maps). The selected instantaneous maps show the velocity vectors at 700 m (dark vectors) and 3500 m (light vectors) superimposed on the 700-m temperature field (solid contours) and 3500-m streamlines (dashed contours). Major peaks in the $(v'T')^{div}$ time series can be associated with baroclinic instability events illustrated in the selected maps. The prevalence of trough events in the study region results in a weak trough feature in the long-term mean Gulf Stream path (see Fig. 1).

APPENDIX A

Mooring Motion Correction

Although stiff, high-performance moorings were used, the drag from the jet caused the moorings to take vertical excursions. The vertical excursions were typically less than 50 m; however, the three southernmost moorings had excursions exceeding 300 m during up to seven events. Therefore, as a first step toward creating regularly gridded data, the mooring measurements were interpolated (and extrapolated) to fixed depths of 400, 700, and 1000 m using a mooring motion correction scheme adapted from Hogg (1991). This scheme, which compensates both the temperature and velocity measurements for mooring motion, assumes that the thickness between any two isotherms is constant so that a canonical temperature profile can be defined:

$$T(p) = F(p - p_{\text{ref}}). \qquad \text{(A1)}$$

In our application of this scheme to the SYNOP data, we used a seventh-order polynomial for the northern moorings, and a ninth-order polynomial for the southern moorings. The zeroth-order coefficient for both polynomials was set to be 12°C; p_{ref} is therefore the pressure of the 12°C isotherm. The remaining coefficients were determined by least squares fitting a subset of the temperature and pressure measurements to the polynomial for the given region. Then, for each mooring, the reference pressure time series was determined by least squares fitting that mooring's daily (T, p) measurements to the polynomial (A1).

In the Hogg (1991) mooring motion correction method, the polynomial (A1) can then be used to determine the compensated temperature T_c at the nominal pressure p_{nom}: $T_c = F(p_{\text{nom}} - p_{\text{ref}})$. We made a slight modification to this temperature correction scheme to ensure that the corrected temperature smoothly approached the measured temperature as the mooring's vertical excursion took a current meter through the nominal level (400 m, 700 m, or 1000 m). Briefly, a weighted average of the corrected temperatures from the two nearest current meters is used to estimate the compensated temperature T_c at the nominal pressure p_{nom}:

$$T_c = w_u \mathcal{T}_u + w_l \mathcal{T}_l, \qquad \text{(A2)}$$

where the subscript c refers to the "compensated" measurement, the subscripts u and l refer to the upper and lower current meter measurements nearest to the nominal pressure p_{nom}, and where

$$\mathcal{T}_u = F(p_{\text{ref}} - p_{\text{nom}}) + (T_u - F(p_{\text{ref}} - p_u))$$

$$\mathcal{T}_l = F(p_{\text{ref}} - p_{\text{nom}}) + (T_l - F(p_{\text{ref}} - p_l))$$

$$w_u = \frac{|p_l - p_{\text{nom}}|}{|p_{\text{nom}} - p_u| + |p_{\text{nom}} - p_l|}$$

$$w_l = \frac{|p_{\text{nom}} - p_u|}{|p_{\text{nom}} - p_u| + |p_{\text{nom}} - p_l|}.$$

This modification (A2) to Hogg's (1991) temperature correction method (A1) relaxes the parallel isotherm restriction and forces the corrected temperature T_c to smoothly approach the measured temperature T_{meas} when the current meter pressure p_{meas} approaches the nominal pressure p_{nom}: when $p_{\text{meas}} = p_{\text{nom}}$, $T_c = T_{\text{meas}}$.

The velocity measurements were also compensated for mooring motion by using Hogg's (1991) procedure of interpolating or extrapolating on temperature:

$$u_c = \frac{u_u - u_l}{T_u - T_l}(T_c - T_l) + u_l$$

$$v_c = \frac{v_u - v_l}{T_u - T_l}(T_c - T_l) + v_l,$$

where again, the subscript c refers to the compensated measurement, and the subscripts u and l refer to the nearest upper and lower current meter measurements on the same mooring. Unlike interpolating the velocity on depth, this velocity interpolation scheme is consistent with the thermal wind. Further details of the mooring motion correction procedure are described in Cronin et al. (1992).

A convenient feature of the mooring motion compensation scheme is the equivalence of the reference pressure p_{ref} to the inverted echo sounder measurement of the depth of the 12°C isotherm (suitably scaled by a factor of 1.01 db m^{-1}). Thus, the IES p_{ref} can be used in the canonical profile (13) to estimate the temperature time series at each IES site for the depths of 400, 700, and 1000 m. This method of using IESs to estimate temperature has been verified by direct comparison at the central 12 sites for both years by Cronin et al. (1992). Because the IES array was larger than the current meter array, temperature estimates from the peripheral IESs essentially double the area in which the temperature field can be adequately mapped.

APPENDIX B

Error Analysis

At the measurement sites the optimally interpolated (OI) data matches the measured data to within the prescribed measurement error, and away from the sites, the error in the OI field increases. The question addressed in this appendix is: How does the measurement error and interpolation/extrapolation affect the statistics (means, variances, and co-

variances), the gradients, and the products of these quantities? That is, what is the measurement error of the mapped energy transfer rates? This question is distinct from the question of how representative the statistics are of their true expectation value. To the degree that the measurement error is negligible, the measured statistics are representative of the 26-month experiment period, although, depending upon the statistical error, they may not represent the limit as the averaging period approaches infinity. Our focus is upon the energy exchanges that occurred during this experiment, and consequently the measurement error was used to estimate the errors in the computed terms.

For each of the daily maps, the OI produces an estimate of the fractional error in the mapped field using information on the sensor's measurement error, the correlation length scale, and the gridpoint's location relative to the set of measurement sites (Bretherton et al. 1976; Freeland and Gould 1976). To remain general, in the following discussion, $\hat{\theta}$ will be the OI least squares estimator of the true value of the random Gaussian variable θ with zero mean and variance σ_θ^2. The OI error estimate $(\mathrm{er}(\hat{\theta}))^2/\sigma_\theta^2 = (\hat{\theta} - \theta)^2/\sigma_\theta^2$ can be used to estimate the error in the variance of $\hat{\theta}$ by assuming that θ has a joint Gaussian distribution (Bendat and Piersol 1986, p. 151) and therefore

$$\begin{aligned}\mathrm{er}(\hat{\theta}^2)^2 &= \overline{(\hat{\theta}^2 - \theta^2)^2} \\ &= 3\overline{\hat{\theta}^2}^2 - 2\overline{\hat{\theta}^2\theta^2} - 4\overline{\hat{\theta}\theta}^2 + 3\overline{\theta^2}^2,\end{aligned}$$

which, noting that $\hat{\theta}$ is a least squares estimator, $[\overline{(\hat{\theta} - \theta)\hat{\theta}} = 0]$ can be simplified to

$$\mathrm{er}(\hat{\theta}^2)/\sigma_\theta^2 = (\mathrm{er}(\hat{\theta})/\sigma_\theta)\sqrt{4 - (\mathrm{er}(\hat{\theta})/\sigma_\theta)^2}. \quad \text{(B1)}$$

The error in the mean variance [i.e., $\mathrm{er}(\overline{u'u'})$, $\mathrm{er}(\overline{v'v'})$, $\mathrm{er}(\overline{T'T'})$] can be estimated as

$$\mathrm{er}(\overline{\hat{\theta}^2}) = \frac{1}{\sqrt{N}}\sqrt{\frac{1}{N}\sum (\mathrm{er}(\hat{\theta}^2))^2}, \quad \text{(B2)}$$

where N is the number of independent measurements. Because the original data were 48-hour low-pass filtered, N is set as one-half the total number of daily maps. The characteristic variance for each variable (σ_u^2, σ_v^2, σ_T^2) was estimated as the median of the mapped variance within the region of accurate mapping.

The measurement error in the mapped covariance fields (e.g., $\overline{u'v'}$) can be estimated by noting that $\overline{u'v'} = \gamma_{uv}\sqrt{\overline{u'u'}}\sqrt{\overline{v'v'}}$, where γ_{uv} is the correlation coefficient between variables u' and v'. Thus,

$$\begin{aligned}\mathrm{er}(\overline{u'v'}) &= \sqrt{\overline{u'u'}}\,\gamma_{uv}\mathrm{er}(\sqrt{\overline{v'v'}}) + \sqrt{\overline{v'v'}}\,\gamma_{uv}\mathrm{er}(\sqrt{\overline{u'u'}}) \\ &\quad + \sqrt{\overline{u'u'}}\sqrt{\overline{v'v'}}\,\mathrm{er}(\gamma_{uv}) \\ &= \frac{1}{2}\left(\sqrt{\overline{u'u'}}\,\gamma_{uv}\frac{\mathrm{er}(\overline{v'v'})}{\sqrt{\overline{v'v'}}} + \sqrt{\overline{v'v'}}\,\gamma_{uv}\frac{\mathrm{er}(\overline{u'u'})}{\sqrt{\overline{u'u'}}}\right) \\ &\quad + \sqrt{\overline{u'u'}}\sqrt{\overline{v'v'}}\,\mathrm{er}(\gamma_{uv}) \\ &\approx \frac{1}{2}\overline{u'v'}\left(\frac{\mathrm{er}(\overline{u'u'})}{\sigma_u^2} + \frac{\mathrm{er}(\overline{v'v'})}{\sigma_v^2}\right) \\ &\quad + \sqrt{\overline{u'u'}}\sqrt{\overline{v'v'}}\,\mathrm{er}(\gamma_{uv}),\end{aligned}$$

where $\mathrm{er}(\overline{u'u'})/\sigma_u^2$ and $\mathrm{er}(\overline{v'v'})/\sigma_u^2$ are estimated from the OI fractional error using (B1)–(B2), and $\overline{u'v'}$ is estimated as the median of $|\overline{u'v'}|$ from the region that had low errors in both $\overline{u'u'}$ and $\overline{v'v'}$. The $\mathrm{er}(\gamma_{uv})$ is a statistical error that depends upon the probability distribution and degrees of freedom. Therefore, for the measurement error estimate, $\mathrm{er}(\gamma)$ is ignored, and the covariance measurement error reduces to

$$\mathrm{er}(\overline{u'v'}) \approx \frac{1}{2}\overline{u'v'}\left(\frac{\mathrm{er}(\overline{u'u'})}{\sigma_u^2} + \frac{\mathrm{er}(\overline{v'v'})}{\sigma_v^2}\right).$$

Similar relations can be written for $\mathrm{er}(\overline{u'T'})$ and $\mathrm{er}(\overline{v'T'})$.

Likewise, letting $\overline{u'v'v'} = \gamma_{uvv}\sqrt{\overline{u'u'}}\,\overline{v'v'}$, it can be shown that the measurement error in the triple covariance $\overline{u'v'v'}$ (again ignoring the statistical errors) is

$$\mathrm{er}(\overline{u'v'v'}) \approx \frac{1}{2}\overline{u'v'v'}\left(\frac{\mathrm{er}(\overline{u'u'})}{\sigma_u^2} + 2\frac{\mathrm{er}(\overline{v'v'})}{\sigma_v^2}\right).$$

Similar relations can be made for $\mathrm{er}(\overline{u'u'u'})$, $\mathrm{er}(\overline{v'u'u'})$, $\mathrm{er}(\overline{v'v'v'})$, $\mathrm{er}(\overline{u'T'T'})$, and $\mathrm{er}(\overline{v'T'T'})$.

Away from the measurement sites, the OI output fields can have bias errors as well as the variance errors. Although the OI procedure cannot estimate bias errors, an estimate of the bias errors can be made by systematically leaving out sites in the OI processing and comparing the OI output fields with the measured data. Doing this, we found that the bias was typically 20% of the OI estimated error field. These biases are equivalent to the measurement error in the mean field. Thus, we have estimated

$$\mathrm{er}(\bar{u}) = 0.2\sqrt{\mathrm{er}(u')^2}$$

$$\mathrm{er}(\bar{v}) = 0.2\sqrt{\mathrm{er}(v')^2}$$

$$\mathrm{er}(\bar{T}) = 0.2\sqrt{\mathrm{er}(T')^2}.$$

In order to remain general, we will consider a term that is a function of the statistical quantities $q_1, q_2, \ldots$: term $= f(q_1, q_2, \cdots)$. The error in this term can be estimated using the chain rule according to

$$\mathrm{er(term)} = \sqrt{\left(\frac{\partial f}{\partial q_1}\,\mathrm{er}(q_1) + \frac{\partial f}{\partial q_2}\,\mathrm{er}(q_2) + \cdots\right)^2}$$

$$= \sqrt{\left(\frac{\partial f}{\partial q_1}\,\mathrm{er}(q_1)\right)^2 + \left(\frac{\partial f}{\partial q_2}\,\mathrm{er}(q_2)\right)^2 + 2\,\frac{\partial f}{\partial q_1}\frac{\partial f}{\partial q_2}\,\overline{\mathrm{er}(q_1)\mathrm{er}(q_2)} + \cdots}.$$

If the errors in the statistics $q_1, q_2, \ldots$ are uncorrelated, then the error in the term reduces to

$$\mathrm{er(term)} = \sqrt{\left(\frac{\partial f}{\partial q_1}\,\mathrm{er}(q_1)\right)^2 + \left(\frac{\partial f}{\partial q_2}\,\mathrm{er}(q_2)\right)^2 + \cdots}. \tag{B3}$$

For example, the error in the central finite difference approximation of the gradients $\partial q/\partial x$ and $\partial q/\partial y$ can be estimated as

$$\mathrm{er}(q_x) = \frac{1}{2\Delta x}\sqrt{\mathrm{er}(q(x-\Delta x, y))^2 + \mathrm{er}(q(x+\Delta x, y))^2}$$

$$\mathrm{er}(q_y) = \frac{1}{2\Delta y}\sqrt{\mathrm{er}(q(x, y-\Delta y))^2 + \mathrm{er}(q(x, y+\Delta y))^2}.$$

Note that if the errors in q are correlated over the 40 km ($2\Delta x$, $2\Delta y$) finite difference range, these expressions will be an overestimate of the error in the gradients (Kim and Watts 1995).

The relative errors in the mapped terms can be estimated using (B3) and noting that

$$\bar{\mathbf{u}}\cdot\nabla\mathrm{EPE} = f\left(\bar{u}, \bar{v}, \frac{\partial\overline{T'T'}}{\partial x}, \frac{\partial\overline{T'T'}}{\partial y}\right)$$

$$-\frac{g\alpha}{\theta_z}\,\overline{\mathbf{u}'T'}\cdot\nabla\bar{T} = f\left(\overline{u'T'}, \overline{v'T'}, \frac{\partial\bar{T}}{\partial x}, \frac{\partial\bar{T}}{\partial y}\right)$$

$$\nabla\cdot\overline{\mathbf{u}'\mathrm{EPE}'} = f\left(\frac{\partial\overline{u'T'T'}}{\partial x}, \frac{\partial\overline{v'T'T'}}{\partial y}\right)$$

$$g\alpha\overline{w'\mathrm{T}'} = f\left(\bar{\mathbf{u}}\cdot\nabla\mathrm{EPE}, -\frac{g\alpha}{\theta_z}\,\overline{\mathbf{u}'T'}\cdot\nabla\bar{T}, \nabla\cdot\overline{\mathbf{u}'\mathrm{EPE}'}\right)$$

$$\overline{u'u'}\frac{\partial\bar{u}}{\partial x} + \overline{u'v'}\left(\frac{\partial\bar{u}}{\partial y} + \frac{\partial\bar{v}}{\partial x}\right) + \overline{v'v'}\frac{\partial\bar{v}}{\partial y} = f\left(\overline{u'u'}, \overline{u'v'}, \overline{v'v'}, \frac{\partial\bar{u}}{\partial x}, \frac{\partial\bar{u}}{\partial y}, \frac{\partial\bar{v}}{\partial x}, \frac{\partial\bar{v}}{\partial y}\right)$$

$$\bar{\mathbf{u}}\cdot\nabla\mathrm{EKE} = f(\bar{u}, \bar{v}, \overline{u'u'}, \overline{v'v'})$$

$$\nabla\cdot\overline{\mathbf{u}'\mathrm{EKE}'} = f\left(\frac{\partial\overline{u'u'u'}}{\partial x}, \frac{\partial\overline{u'v'v'}}{\partial x}, \frac{\partial\overline{v'u'u'}}{\partial y}, \frac{\partial\overline{v'v'v'}}{\partial y}\right)$$

$$\frac{g\alpha}{\theta_z}\,\overline{\mathbf{u}'T'}^{\mathrm{div}}\cdot\nabla\bar{T} = f\left(\overline{u'T'}^{\mathrm{div}}, \overline{v'T'}^{\mathrm{div}}, \frac{\partial\bar{T}}{\partial x}, \frac{\partial\bar{T}}{\partial y}\right)$$

$$\overline{u'T'}^{\mathrm{div}} = f\left(\overline{u'T'}, \frac{\partial\overline{T'T'}}{\partial y}\right)$$

$$\overline{v'T'}^{\mathrm{div}} = f\left(\overline{v'T'}, \frac{\partial\overline{T'T'}}{\partial x}\right).$$

The mapped fields in Figs. 3–13 are darkly shaded where the measurement error (B3) is equal to or larger than the signal, and lightly shaded where the error is greater than 50% of the estimated term.

REFERENCES

Bendat, J. S., and A. G. Piersol, 1986: *Random Data.* Wiley and Sons, 566 pp.

Bower, A. S., and T. Rossby, 1989: Evidence of cross-frontal exchange processes in the Gulf Stream based on isopycnal RAFOS float data. *J. Phys. Oceanogr.*, **19,** 1177–1190.

Bretherton, F. P., R. E. Davis, and C. B. Fandry, 1976: A technique for objective analysis and design of oceanographic experiments applied to MODE-73. *Deep Sea Res.*, **23,** 559–582.

Bryden, H. L., 1982: Sources of eddy energy in the Gulf Stream recirculation region. *J. Mar. Res.*, **40,** 1047–1068.

Charney, J. G., 1947: The dynamics of long waves in a baroclinic westerly current. *J. Meteor.*, **4,** 135–163.

Cornillon, P., 1986: The effect of the New England seamounts on Gulf Stream meandering as observed from satellite IR imagery. *J. Phys. Oceanogr.*, **16,** 386–389.

Cronin, M., 1993: Eddy–mean flow interaction in the Gulf Stream at 68°W. Ph.D. dissertation, University of Rhode Island, 118 pp.

——, 1996: Eddy–mean flow interaction in the Gulf Stream at 68°W. Part II: Eddy forcing on the time-mean flow. *J. Phys. Oceanogr.*, **26,** 2132–2151.

——, K. L. Tracey, and D. R. Watts, 1992: Mooring motion correction of the SYNOP Central Array current meter data. GSO Tech. Rep. No. 92-4, University of Rhode Island, Kingston, RI, 114 pp.

Dewar, W. K., and J. M. Bane, 1989: Gulf Stream dynamics. Part II: Eddy energetics at 73°W. *J. Phys. Oceanogr.*, **19,** 1574–1587.

Eady, E. T., 1949: Long waves and cyclone waves. *Tellus,* **1,** 35–52.

Fofonoff, N., 1969: Spectral characteristics of internal waves in the ocean. *Deep-Sea Res.,* **16**(Suppl.), 58–71.

Freeland, H. J., and W. J. Gould, 1976: Objective analysis of mesoscale ocean circulation features. *Deep-Sea Res.,* **23,** 915–923.

Gill, A. E., 1982: *Atmosphere–Ocean Dynamics.* Academic Press, 662 pp.

Halkin, D., T. A. Rago, and T. Rossby, 1985: Data report of the Pegasus Program at 73W. Tech. Rep. 85-2, University of Rhode Island, Kingston, RI, 198 pp.

Hall, M. M., 1986: Assessing the energetics and dynamics of the Gulf Stream at 68°W from moored current measurements. *J. Mar. Res.,* **44,** 423–433.

Hogg, N. G., 1991: Mooring motion corrections revisited. *J. Atmos. Oceanic Technol.,* **8,** 289–295.

——, 1992: On the transport of the Gulf Stream between Cape Hatteras and the Grand Banks. *Deep-Sea Res.,* **39,** 1231–1246.

Illari, L., and J. Marshall, 1983: On the interpretation of eddy fluxes during a blocking episode. *J. Atmos. Sci.,* **40,** 2232–2242.

Johns, E., and R. J. Zantopp, 1991: The SYNOP experiment: Moored acoustic Doppler current meter profiler data for the period June 1988 to August 1990. University of Miami RSMAS Tech. Rep. No. 91-003, 130 pp.

——, D. R. Watts, and H. T. Rossby, 1989: A test of geostrophy in the Gulf Stream. *J. Geophys. Res.,* **94,** 3211–3222.

Kim, H. S., and D. R. Watts, 1994: An observational streamfunction in the Gulf Stream. *J. Phys. Oceanogr.,* **24,** 2639–2657.

Kontoyiannis, H., 1996: Quasi-geostrophic modeling of mixed instabilities in the Gulf Stream near 73W. *Dyn. Atmos. Oceans,* in press.

——, and D. R. Watts, 1994: Observations on the variability of the Gulf Stream path between 74W and 70W. *J. Phys. Oceanogr.,* **24,** 1999–2012.

Lau, N.-C., and J. Wallace, 1979: On the distribution of horizontal transports by transient eddies in the Northern Hemisphere wintertime circulation. *J. Atmos. Sci.,* **36,** 1844–1861.

Lee, T., 1994: Variability of the Gulf Stream path observed from satellite infrared images. Ph.D. dissertation, University of Rhode Island, 188 pp.

Lindstrom, S. S., and D. Randolph Watts, 1994: Vertical motion in the Gulf Stream. *J. Phys. Oceanogr.,* **24,** 2321–2333.

Marshall, J., and G. Shutts, 1981: A note on rotational and divergent eddy fluxes. *J. Phys. Oceanogr.,* **11,** 1677–1680.

Pedlosky, J., 1987: *Geophysical Fluid Dynamics.* Springer-Verlag, 710 pp.

Plumb, R. A., 1983: A new look at the energy cycle. *J. Atmos. Sci.,* **40,** 1670–1688.

Qian, X. S., and D. R. Watts, 1992: The SYNOP experiment: Bottom pressure maps for the Central Array May 1988 to August 1990, GSO Tech. Rep. No. 92-3, University of Rhode Island, Kingston, RI, 185 pp.

Rossby, T., 1987: On the energetics of the Gulf Stream at 73°W. *J. Mar. Res.,* **45,** 59–82.

Shay, T. J., S. Haines, J. M. Bane, and D. R. Watts, 1992: SYNOP Central Array current meter data report: Mooring period May 1988–September 1990. University of North Carolina Tech. Rep. CMS 91–2, 106 pp.

——, J. M. Bane, D. R. Watts, and K. L. Tracey, 1995: Gulf Stream flow field and events near 68W. *J. Geophys. Res.,* **100,** 22 565–22 589.

Tracey, K. L., and D. R. Watts, 1991: The SYNOP experiment: Thermocline depth maps for the Central Array October 1987 to August 1990. GSO Tech. Rep. 91-5, University of Rhode Island, Kingston, RI, 193 pp.

Watts, D. R., 1983: Gulf Stream variability. *Eddies in Marine Science,* A. R. Robinson, Ed., Springer-Verlag, 114–144.

——, 1985: Gulf Stream workshop proceedings Tech. Rep., University of Rhode Island, Kingston, RI, 571 pp.

——, and H. T. Rossby, 1977: Measuring dynamic heights with inverted echo sounders: Results from MODE. *J. Phys. Oceanogr.,* **7,** 345–358.

——, J. M. Bane, K. L. Tracey, and T. J. Shay, 1995: Gulf Stream path and thermocline structure near 74W and 65W. *J. Geophys. Res.,* **100,** 18 291–18 312.